frontiers | Frontiers in Earth Science

ORIGINAL RESEARCH
published: 03 May 2022
doi: 10.3389/feart.2022.893751

Late Paleozoic Shoshonitic Magmatism in the Southwestern Middle Tianshan (Tajikistan) of the Southwestern Altaids: Implications for Slab Roll-Back With Extensional Arc-Related Basins After Flat Subduction

Gufron Khalimov[1,2,3,4], *He Yang*[1,2,3]*, *Miao Sang*[1,3]*, *Wenjiao Xiao*[1,2,3]*, *Yunus Mamadjanov*[4,5], *Jovid Aminov*[4], *Dzhovid Yogibekov*[1,2,3] and *Xijun Liu*[1,6]

[1]Xinjiang Research Center for Mineral Resources, Xinjiang Institute of Ecology and Geography, Chinese Academy of Sciences, Urumqi, China, [2]College of Earth and Planetary Sciences, University of Chinese Academy of Sciences, Beijing, China, [3]Xinjiang Key Laboratory of Mineral Resources and Digital Geology, Urumqi, China, [4]Institute of Geology, Earthquake Engineering and Seismology, National Academy of Sciences of Tajikistan, Dushanbe, Tajikistan, [5]Research Center for Ecology and Environment of Central Asia, Chinese Academy of Sciences, Dushanbe, Tajikistan, [6]Guangxi Key Laboratory of Hidden Metallic Ore Deposits Exploration, College of Earth Sciences, Guilin University of Technology, Guilin, China

Paleozoic magmatic rocks are widespread in the western Middle Tianshan. Their petrogenesis can provide important insights into the geodynamic evolution of the southwestern Altaids. Here, we present an integrated study of U–Pb zircon geochronology and geochemical and Lu–Hf isotopic compositions for the Late Paleozoic shoshonitic Chorukhdairon pluton and genetically and spatially related quartz porphyry in the southern Chatkal–Kurama terrane, western Middle Tianshan. The Chorukhdairon pluton mainly comprises monzodiorite and quartz monzodiorite (first phase), quartz monzonite (second and main phase), monzogranite (third phase), and leucomonzogranite (fourth phase). LA–ICP–MS zircon dating yielded magma crystallization ages of 294–291 Ma and 286 Ma for the Chorukhdairon pluton and quartz porphyry, respectively. All the rocks possess high K_2O content (3.29–5.90 wt.%) and show an affinity with shoshonite series rocks. They display similar trace element compositions characterized by the enrichment of large ion lithophile elements (e.g., Rb, Th, U, and K) and depletion of high-field strength elements (e.g., Nb, Ta, P, and Ti), compatible with typical arc magmatism. Combined with zircon Lu–Hf isotopic data, we suggest that the Chorukhdairon pluton was produced by partial melting of the enriched mantle, followed by fractional crystallization of pyroxenes, amphibole, plagioclase, biotite, and accessory Fe–Ti oxides, apatite, and zircon. The quartz porphyries are similar to highly fractionated I-type granitic rocks, and their parental magma could result from the mixing of different batches of mantle-derived magmas or magmas derived from the mantle and juvenile lower crust. Considering the continuousness of the Middle Carboniferous to Early Permian magmatism in the western Middle Tianshan

OPEN ACCESS

Edited by:
Hanlin Chen,
Zhejiang University, China

Reviewed by:
Yingde Jiang,
Guangzhou Institute of Geochemistry (CAS), China
Tim Kusky,
China University of Geosciences Wuhan, China

***Correspondence:**
He Yang
hyang@ms.xjb.ac.cn
Miao Sang
sangmiao@ms.xjb.ac.cn
Wenjiao Xiao
wj-xiao@mail.iggcas.ac.cn

Specialty section:
This article was submitted to Structural Geology and Tectonics, a section of the journal Frontiers in Earth Science

Received: 10 March 2022
Accepted: 31 March 2022
Published: 03 May 2022

Citation:
Khalimov G, Yang H, Sang M, Xiao W, Mamadjanov Y, Aminov J, Yogibekov D and Liu X (2022) Late Paleozoic Shoshonitic Magmatism in the Southwestern Middle Tianshan (Tajikistan) of the Southwestern Altaids: Implications for Slab Roll-Back With Extensional Arc-Related Basins After Flat Subduction. Front. Earth Sci. 10:893751. doi: 10.3389/feart.2022.893751

and other regional geological data, we suggest that the Chorukhdairon pluton and related quartz porphyry probably formed in an oceanic subduction setting. Furthermore, the temporal and spatial evolution of the Paleozoic magmatism imply that the flat-slab subduction that was induced by the subduction/accretion of seamounts probably occurred beneath the Middle Tianshan during the Middle Devonian to Early Carboniferous, after which the southeastward slab roll-back occurred during the Middle Carboniferous to Early Permian. The late slab roll-back was responsible for the southeastward arc magmatism migration and magmatic flare-up in the Chatkal–Kurama terrane, western Tianshan, and led to the formation of arc-related extensional basins and significant crustal growth in the southwestern Altaids.

Keywords: shoshonitic magmatism, petrogenesis, flat subduction, slab roll-back, Middle Tianshan

INTRODUCTION

The evolution of the accretionary orogenic belts is characterized by multiple arc generation and arc-continent (or-arc) amalgamation (Condie, 2007; Windley et al., 2007; Cawood et al., 2009; Xiao et al., 2015). Magmatism within arcs records the thermal evolution of the sub-arc mantle and can be used to trace the deep dynamic processes, such as slab roll-back, flat-slab subduction, ridge subduction, slab tearing, slab break-off, and removal of deep lithosphere beneath arcs by delamination (Guivel et al., 2006; Ferrari et al., 2007; DeCelles et al., 2009; Windley and Xiao, 2018; Chapman and Ducea, 2019).

The Altaids or Central Asian Orogenic Belt, which is surrounded by Siberia, Baltica, Karakum, Tarim, and North China cratons (**Figure 1A**), is one of the largest accretionary belts on Earth and represents the largest site of Phanerozoic juvenile crustal growth in

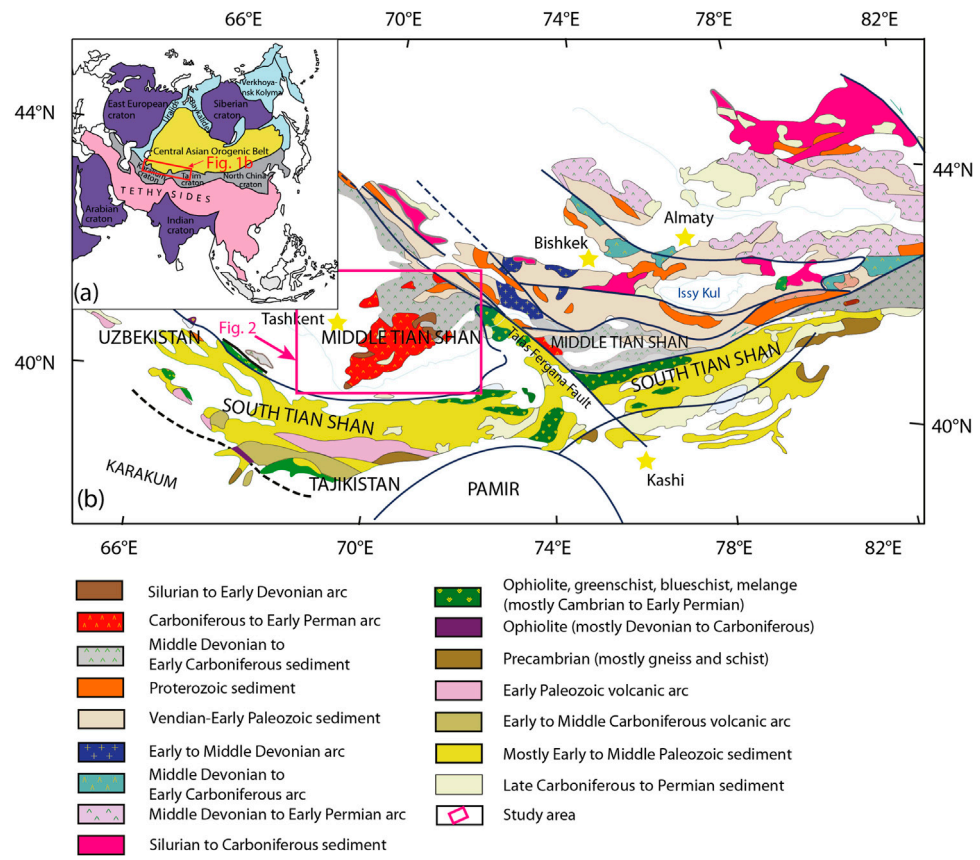

FIGURE 1 | (A) Geological sketch map showing the position of the Central Asian Orogenic Belt and **(B)** Geological and tectonic map of the western Tianshan orogen (modified after Xiao et al. (2013)).

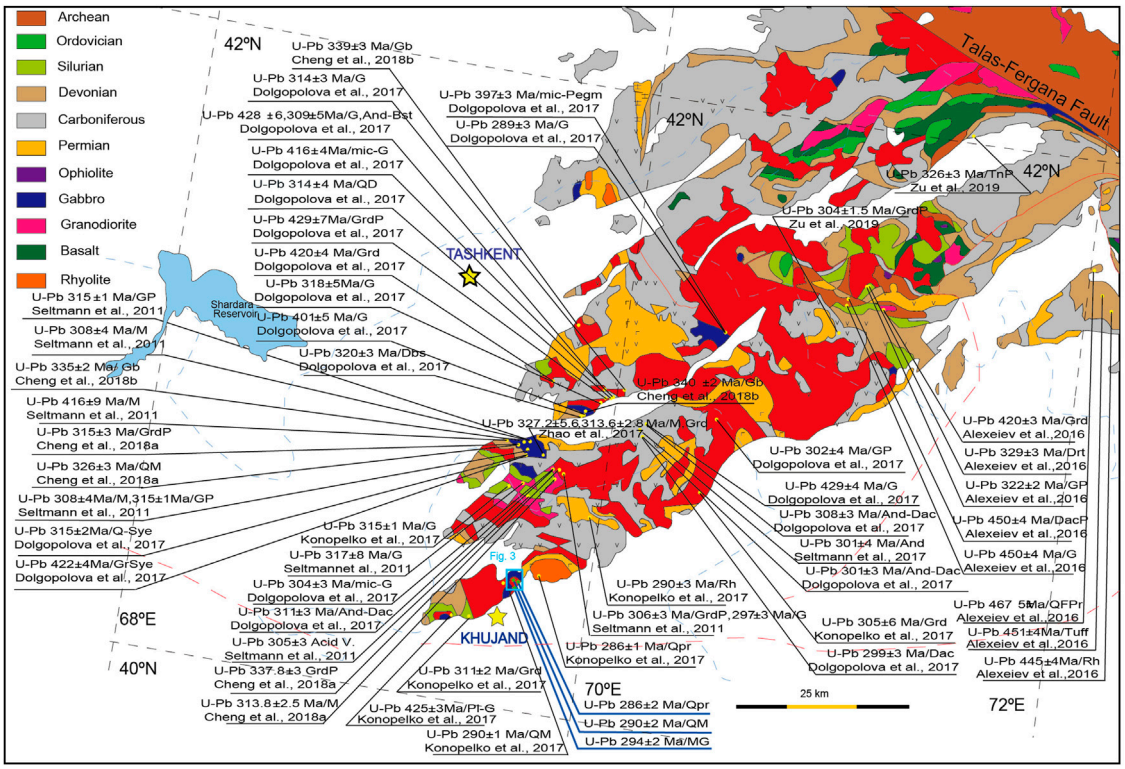

FIGURE 2 | Simplified geological map of the Chatkal–Kurama terrane of the Middle Tianshan and the reported ages for the Paleozoic magmatic rocks. G, granite; MG, monzogranite; Grd, granodiorite; Drt, diorite; QD, quartz diorite; TnP, tonalite porphyry; Sye, syenite; Q-Sye, quartz syenite; GrSye, granosyenite; M, monzonite; QM, quartz monzonite; Gb, gabbro; Dbs, diabase; GP, granite porphyry; GrdP, granodiorite porphyry; Bst, basalt; And, andesite; Dac, dacite; Rh, rhyolite; Acid V., acid volcanic; Qpr, quartz porphyry; QFPr, quartz–feldspar porphyry; mic-G, microgranite-porphyry; DacP, dacite-porphyry; mic-Pegm, micropegmatite; Pl-G, plagiogranite.

the world (Şengör et al., 1993; Jahn, 2004; Windley et al., 2007; Xiao et al., 2015; Tang et al., 2017). The Altaids comprises a collage of oceanic-islands, continental-margin arcs, seamounts, accretionary wedges, ophiolitic mélanges, and microcontinents that amalgamated to Asia over ~750 million years during the latest Proterozoic–Early Mesozoic (Şengör et al., 1993; Windley et al., 2007; Xiao et al., 2015). Its formation was mainly controlled by the subduction and closure of the Paleo-Asian Ocean and arc-related basins. The Tianshan orogenic belt is located at the southwestern margin of the Altaids and recorded the final evolutionary history of the Altaids (**Figure 1**). It stretches ~2,500 km from central Uzbekistan to eastern Xinjiang and formed due to the convergence between the Karakum–Tarim cratons and the southern accretionary margin of the Siberia Craton and the Paleo-Kazakhstan continent (Biske and Seltmann, 2010; Burtman, 2010; Xiao et al., 2013; Alexeiev et al., 2016; Worthington et al., 2017; Sang et al., 2018). The NW–SE-trending dextral Talas–Fergana fault (TFF) cuts the western part of the Tianshan, resulting in a dramatic dextral transcurrent motion in the Late Paleozoic to Early Mesozoic (Worthington et al., 2017). Relative to the eastern part of the Tianshan, the studies on subduction, accretion, and collision processes in the western Tianshan are relatively less systematical, especially for those parts in Tajikistan and Uzbekistan. Importantly, the complex slab dynamic processes in the western Tianshan have not been well constrained.

The Chatkal–Kurama terrane constitutes the major component of the western Middle Tianshan arc west to the Talas–Fergana fault and is characterized by the outcrop of voluminous Paleozoic volcano-plutonic rocks (**Figures 1**, **2**). The Chatkal–Kurama terrane records considerable episodes of continental growth and crustal reworking during the Early to Late Paleozoic, which can provide insights into the tectonic evolution and slab dynamic processes related to the subduction and consumption of the southwestern Paleo-Asian ocean. In this contribution, we present a detailed U–Pb zircon geochronological, geochemical, and Lu–Hf isotopic study for the Late Paleozoic Chorukhdairon shoshonitic rocks and related quartz porphyry in the southern Chatkal–Kurama terrane, western Middle Tianshan. These data, together with the previously reported data, are used to discuss the magma sources and evolution processes, magma generation mechanism, and geodynamic evolution of the western Tianshan during the Paleozoic.

GEOLOGICAL SETTING

Traditionally, the Tianshan orogenic belt in Kyrgyzstan, Tajikistan, and Uzbekistan can be divided, from north to

south, into three parts: North Tianshan (NTS), Middle Tianshan (MTS), and South Tianshan (STS), which are separated by the Nikolaev Line (or Terskey fault) and the northern South Tianshan ophiolite belt (Biske and Seltmann, 2010; Burtman, 2010; Seltmann et al., 2011; Konopelko et al., 2017). The North Tianshan is traditionally considered as an Early Paleozoic continental arc, which was built on a Precambrian basement covered by the Lower Paleozoic deposits and intruded by the Caledonian granitoids, and predominately formed due to the Early Paleozoic northward subduction and subsequent closure of the Terskey Ocean (Konopelko et al., 2017). The South Tianshan includes the ophiolite mélange separating the Tarim–Karakum cratons from the Central or Middle Tianshan (Xiao et al., 2013), which accreted during the subduction and closure of the Turkestan Ocean from the Early Paleozoic to the Late Paleozoic (or even Early Mesozoic). The South Tianshan also contains Paleozoic sedimentary strata, high/ultra-high pressure and medium–high temperature metamorphic rocks, and numerous Early and Late Paleozoic magmatic rocks (Seltmann et al., 2011; Dolgopolova et al., 2017; Käßner et al., 2017; Sang et al., 2017; Worthington et al., 2017; Yang et al., 2020).

In the Middle Tianshan east of the Talas–Fergana fault, the exposed rocks are dominated by the Precambrian basement rocks and Early–Late Paleozoic sedimentary strata (Glorie et al., 2011; Seltmann et al., 2011; Alexeiev et al., 2016; Kröner et al., 2017), and the Paleozoic magmatic rocks are rarely exposed probably due to the amagmatic subduction or the arc destruction by subduction erosion processes (Alexeiev et al., 2016). To the west of the Talas–Fergana Fault, the Middle Tianshan is exposed, mainly represented by the Chatkal–Kurama terrane, which is the eastern part of the Late Paleozoic Kyzylkum–Kurama volcano-plutonic belt composed of calc-alkaline, subalkaline, and alkaline magmatic series (Mamadjanov, 2014). The Kyzylkum part of the belt is currently buried under Meso–Cenozoic deposits and traced from geophysical data and well drilling. The Chatkal–Kurama terrane with an outcrop area of > 30,000 km^2 includes a system of mountain ranges: Kuraminsky with the Mogoltau ridge, Sandalashsky, Pskemsky, Ugamsky, Karzhantau, and the western spurs of the Talas Mountains. This terrane is bounded by the Talas–Fergana fault to the north-east, the Dzhebagly fault zone to the north, and the Karachatyr–Bozbutau zone to the south. The Chatkal–Kurama terrane contains abundant Early–Late Paleozoic arc-related magmatic rocks (Seltmann et al., 2011; Alexeiev et al., 2016; Dolgopolova et al., 2017; Cheng et al., 2018a; Cheng et al., 2018b), which were generated by the northward subduction of the Turkestan oceanic slab. On the southern Chatkal Range, the accreted Karaterek ophiolitic mélange belt is exposed, which forms a tectonic cover overlying the volcano-terrigenous deposits of Silurian age and the olistostrome of Middle Carboniferous age and is overlain by Middle Paleozoic formations (Ivanov et al., 2002; Burtman, 2006; Alexeiev et al., 2016).

Within the Chatkal–Kurama terrane, magmatic formations of the shoshonite–latite series are widely exposed and were identified and studied earlier by Mamadjanov and Tajibaev (1987), Mamadjanov (1995), and Mamadjanov (2004). The shoshonite–latite series is the most fully developed series in the Chorukhdairon volcano-tectonic belt of the northeastern Mogoltau Mountains, where it is represented by the volcanic rocks of shoshonite, latite, quartz–latite composition, forming stratiform strata and vent facies. The small intrusions of monzonite porphyries and shoshonite dykes of the subvolcanic facies are also exposed and genetically related to shoshonites. The volcanic formations of the shoshonite–latite series within the Tajik part of the Chatkal–Kurama terrane are also developed as part of the Adrasman and Tashkesken–Samgar volcanic depressions. The basaltic rocks of the shoshonite series are identified in the Shurabsai Formation. In the Chatkal–Kurama terrane, monzonitic intrusions that are genetically related to the shoshonite–latite series composed the Chorukhdairon, Babaiob, Dzhulbarssotkan, and other plutons. The shoshonite–latite series and associated monzonitic intrusions were mainly formed at the late stage of the development of the Chatkal–Kurama terrane, following the powerful manifestation of the products of mid-Carboniferous calc-alkaline magmatism.

GEOLOGY AND PETROGRAPHY

The Chorukhdairon pluton lies in the Tajik part of the Chatkal–Kurama zone and was recognized as a part of the Chorukhdairon volcano-intrusive complex of Permian age (Baratov, 1976). It occupies the northeastern part of the Mogoltau Mountains and is spatially coexisted with the shoshonite–latite series of the Shurabsai suite and the potassic volcanic or subvolcanic rocks of the Kizilnura suite (**Figure 3**). Structurally, the pluton is confined to a monogenic volcanotectonic trough. The Chorukhdairon pluton shows an irregular shape, somewhat elongated in the southeastern direction, with an exposed area of ~15 km^2. The Chorukhdairon pluton includes monzodiorite and quartz monzodiorite (early phase), quartz monzonite (second and main phase), monzogranite (third phase), and leucomonzogranite (fourth and final phase) (**Figures 3**, **4**). The monzodiorites of the early phase of the southwestern part of the Chorukhdairon massif cut through the shoshonites and latites of the Shurabsai Formation with comagmatic formations, as well as older gabbro and granodiorites of the Middle Carboniferous Karamazar complex. In turn, the monzonitic rocks are intruded by dike-like bodies of potassic quartz porphyries of the Kizilnura Formation. The latter circumstance was documented by drilling wells and mine workings, since the surface is not observed and overlapped by Quaternary deposits. Dykes that are genetically related to monzonitoids include monzodiorite porphyrite, quartz syenite porphyry, monzonitoid aplite, and lamprophyre (Mamadjanov, 2004).

Monzodiorite and quartz monzodiorite of the first phase form the northeastern and southwestern parts of the intrusion (**Figure 3**). The surrounding rocks for them are effusive and subvolcanic rocks of the shoshonite–latite series, and uralite gabbro. Monzodiorites are represented by augite–hypersthene varieties. Monzodiorites are fine-grained, massive, and dark gray, with an ideal monzonitic texture. They are mainly composed of

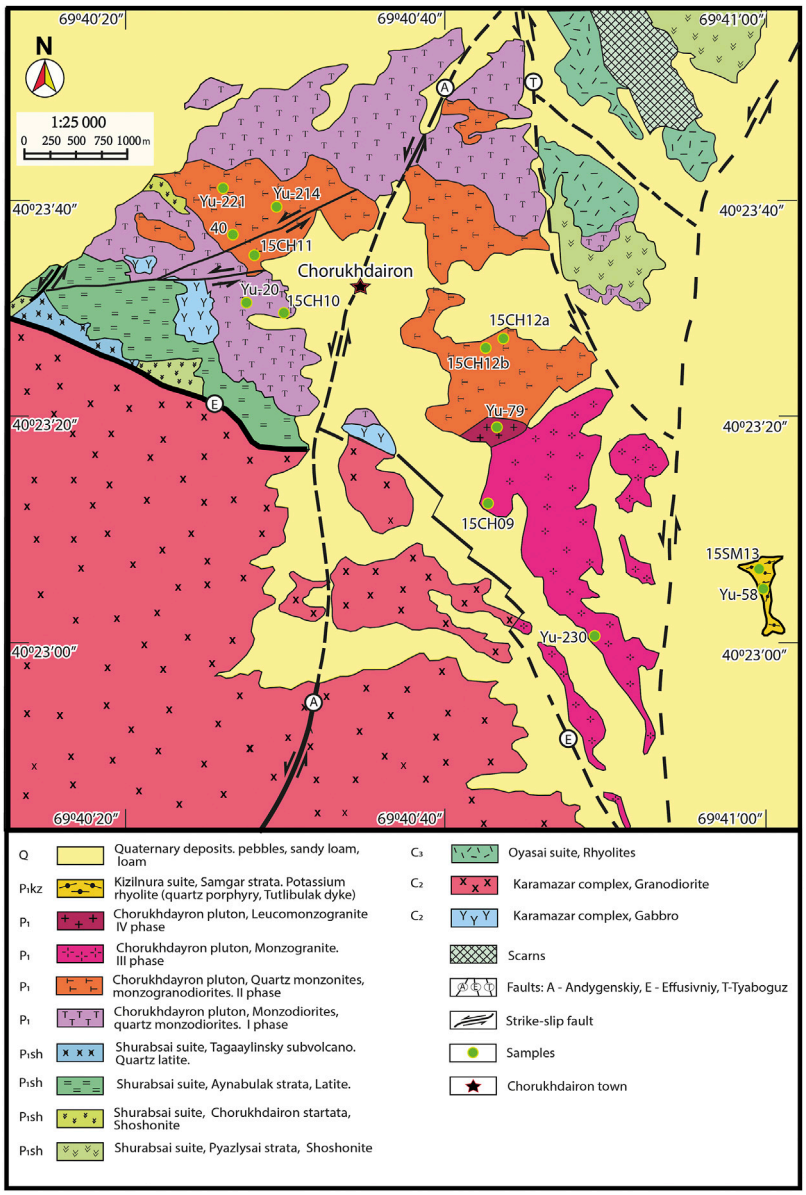

FIGURE 3 | Geological map of the Chorukhdairon pluton (modified after Zaprometov et al. (1973)).

andesine–labradorite (~49.3 vol.%), orthoclase (~21.3 vol.%), quartz (~5.3 vol.%), augite and hypersthene (~19.0 vol.%), and biotite (~1.8 vol.%) (**Figure 5A**). Quartz monzodiorites are fine- to medium-grained in texture and dark gray in color, consisting of andesine–labradorite (~39.4 vol.%), orthoclase (~27.3 vol.%), quartz (~11.5 vol.%), amphibole (~17.6 vol.%), biotite (~1.0 vol.%), and augite (~0.6 vol.%) (**Figure 5B**). The minerals are mostly subhedral and prismatic. The main accessory minerals of the first phase rocks (3.0–3.3 vol.%) are apatite, zircon, and magnetite.

Quartz monzonites of the second phase compose a body elongated in the northwest direction in the central part of the pluton (**Figure 3**). They break through the monzonitoids of the first phase. The western part of this phase is less eroded than the eastern part. The quartz monzonites represent the rocks of the main phase and are interconnected by gradual transitions. Quartz monzonites are medium-grained, light gray to pinkish, and weakly porphyritic rocks. They are characterized by the monzonitic and subhedral granular texture and mainly consist of andesine–labradorite (25.3–30.0 vol.%), orthoclase (40.1–44.0 vol.%), quartz (7.1–23.8 vol.%), augite (0–3.2 vol.%), amphibole (2.6–3.4 vol.%), and biotite (3.5–4.3 vol.%) (**Figures 5C,D**). The accessory minerals (0.9–1.9 vol.%) in the rocks of the main phase are represented by apatite, zircon, magnetite, fluorite, and sphene.

Monzogranites of the third phase are exposed in the southeastern part of the Chorukhdairon pluton, where they

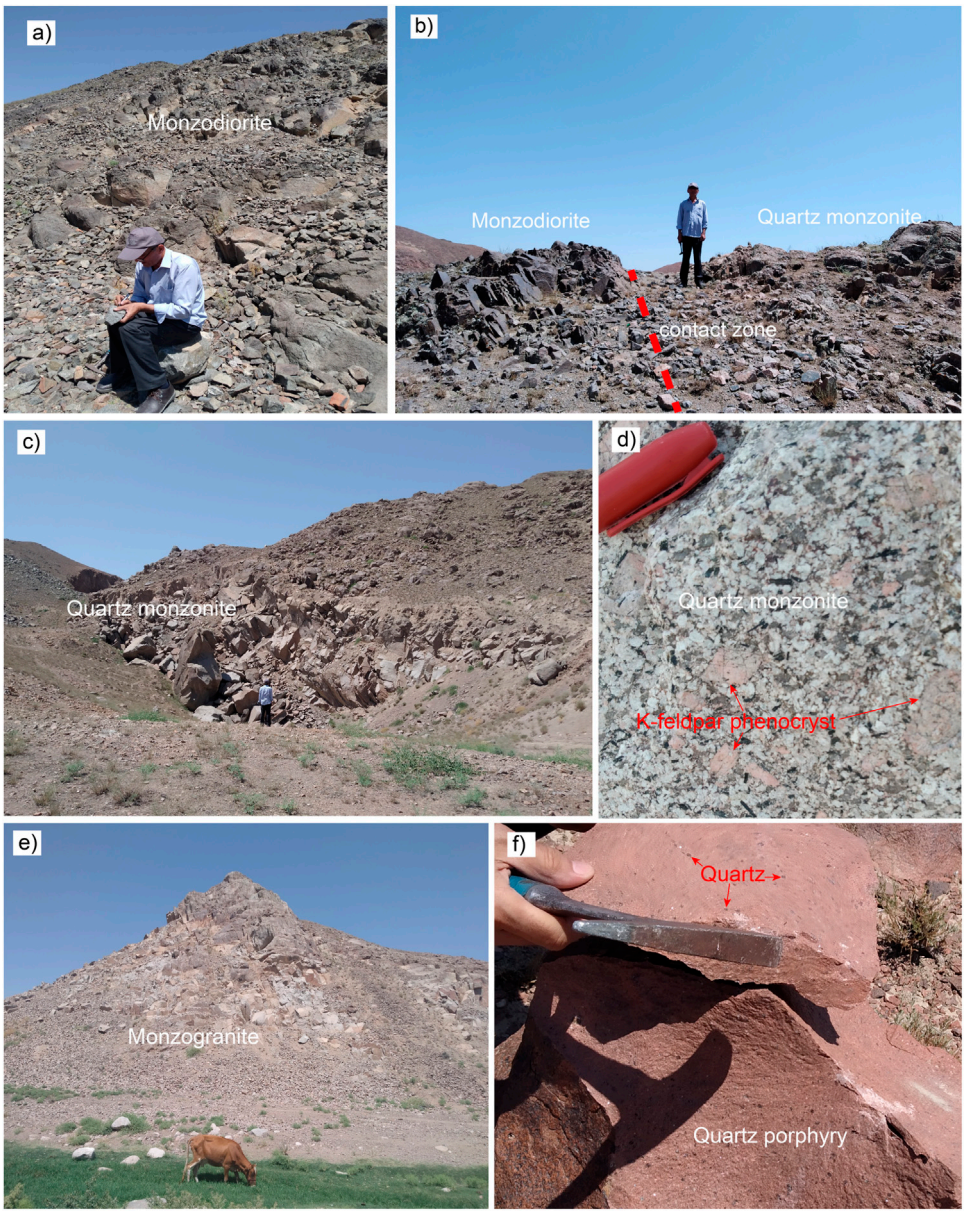

FIGURE 4 | Outcrop photographs of the Chorukhdairon pluton.

compose a large stock-like body (**Figure 3**). In the central part of the pluton, among the monzonitic rocks, there are also small outcrops of monzogranites. Monzogranites are light gray or pinkish, fine to medium-grained porphyritic rocks with a subhedral granular texture. The porphyry nature of monzogranites is due to the presence of large (up to 10 mm) idiomorphic crystals of feldspars, occupying from 10–15% to 25% of the volume. The average mineral composition of monzogranites is as follows: 14.6 vol.% andesine, 52.7 vol.% orthoclase, 27.4 vol.% quartz, 3.5 vol.% biotite, and 1.0 vol.% amphibole (**Figure 5E**). The accessory minerals in monzogranites include magnetite, apatite, zircon, and sphene. Aplites associated with monzogranites of the third phase occur among the related potassium granites, up to 1.0 m thick. Monzogranite-aplites are characterized by the aplite structure and consist of albite (5.0–6.0 vol.%), orthoclase (55–57 vol.%), quartz (30–32 vol.%), and a small amount of hornblende (0.5–1.0 vol.%). Of the accessory minerals (1.5–2.0 vol.%), magnetite, apatite, sphene, and zircon are found in aplites.

Leucomonzogranites of the fourth phase are composed of stock and dyke-like bodies in the central part of the Chorukhdairon pluton (**Figure 3**). Leucomonzogranites are fine-grained, pinkish aplite-like rocks with a fine-grained, anhedral to euhedral granular texture. They consist of andesine (~13.0 vol.%), orthoclase (~52.8 vol.%), quartz (~30.7 vol.%), and biotite (~2.8 vol.%). The accessory minerals are represented by magnetite, zircon, and sphene.

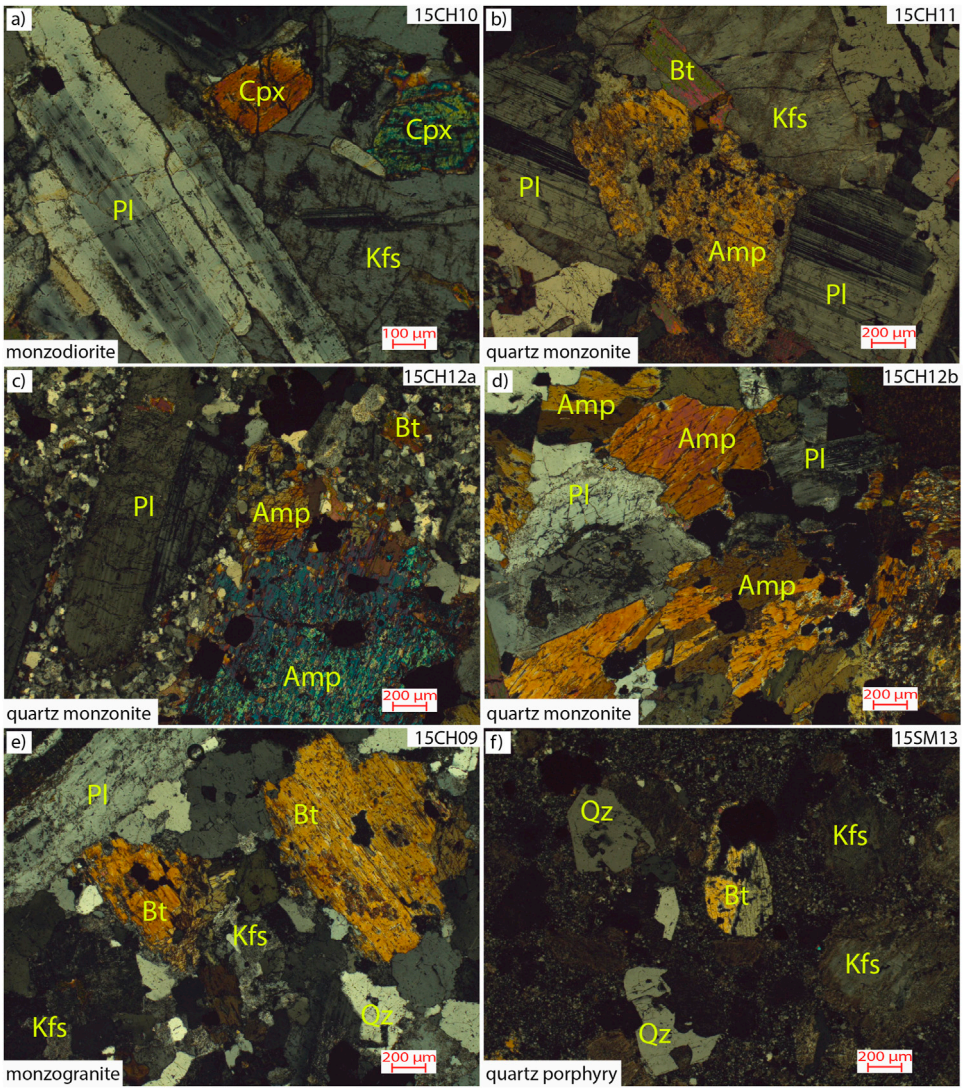

FIGURE 5 | Microphotographs of representative magmatic rocks from the Chorukhdairon pluton.

Within the Chorukhdairon monzonitoid massives, dykes are poorly developed and are represented by monzodiorite-porphyrites, quartz syenite-porphyries, and monzonite-aplite veins. Biotite–augite lamprophyres form a single dyke and complete the shoshonite–latite–monzonitic magmatism of the zone. A clear pattern is observed in the distribution of dykes, expressed in the spatial confinement of individual groups of dyke rocks to the formations of certain phases of the intrusion (Mamadjanov, 1995).

To the eastern part of the Chorukhdairon pluton, along the Khujand–Tashkent highway, the outcrops of subalkaline potassic rhyolites–quartz porphyry that represent the subvolcanic facies of the Kyzylnurinskaya suite are exposed among Quaternary deposits. The outcrop of quartz porphyry is structurally confined to the Tutlybulak fault zone. The Tutlybulak fault is filled with quartz porphyry, with a length of about 6 km and a thickness of up to 200 m. This fault is exposed to the north of the study area and was recorded in the Chorukhdairon area by boreholes. The outcrop of quartz porphyry is characterized by the rocky relief and red coloration against the background of gray proluvial deposits (**Figure 4F**) (Mamadjanov, 2004). The outcrop area of quartz porphyry is small and measures 150–180 × 50–70 m. The quartz porphyry mainly comprises feldspar (55–50 vol.%) and quartz (25–30 vol.%), with minor mica (10 vol.%) and hornblende (5 vol.%).

ANALYTICAL METHODS

Zircon U–Pb Dating

The cathodoluminescence (CL) images of zircons were obtained at the Beijing Geoanalysis Co. Ltd. using JEOL IT-500 SEM equipped with a Delmic CL system. Instrument working conditions are as follows: acceleration voltage of 10 kv; work distance of 16.7 mm; probe current of 63 nA; dwell time of 12 μs.

Zircon U–Pb dating was conducted using LA–ICP–MS at Beijing Geoanalysis Co., Ltd., Beijing, China. The NWR193UC model laser ablation system (Elemental Scientific Lasers LLC, United States) was coupled to an Agilent 7900 ICPMS (Agilent, United States). Detailed tuning parameters can be seen in Thompson et al. (2018). Zircon was mounted in epoxy discs, polished to expose the grains, cleaned ultrasonically in ultrapure water, and then cleaned again prior to the analysis using AR grade methanol. Pre-ablation was conducted for each spot analysis using five laser shots (~0.3 μm in depth) to remove potential surface contamination. The analysis was performed using a 30 μm diameter spot at 6 Hz and a fluence of 4.5 J/cm^2. The iolite software package was used for data reduction (Paton et al., 2010). Zircon GJ-1 and 91500 were used as primary and secondary reference materials, respectively. 91500, GJ-1, and Plesovice were analyzed twice once every 10 analyses of the sample. Typically, 45 s of the sample signals were acquired after 25 s of gas background measurement. The exponential function was used to calibrate the downhole fractionation (Paton et al., 2010). NIST 610 and ^{91}Zr were used to calibrate the trace element concentrations as an external reference material and internal standard element, respectively.

Major and Trace Element Analysis

Thirteen samples from the Chorukhdairon pluton were analyzed for major and trace element composition. The major elements for seven samples (Yu-20, Yu-214, Yu-221, Yu-230, Yu-79, Yu-84, and Yu-58) were determined using the classical silicate method of analysis in the laboratory of physical and mechanical methods of analysis of the former Institute of Geology of the Academy of Sciences of the Republic of Tajikistan, now known as the Institute of Geology, Seismic Construction and Seismology of the National Academy of Sciences of Tajikistan. Their trace elements were analyzed using an inductively coupled plasma mass spectrometer (ICP-MS) at the Key Laboratory of Continental Collision and Plateau Uplift, ITPCAS. A measure of 50 mg of whole-rock powder were dissolved using HF + HNO_3 for trace element determination. The sample pretreatment procedure for trace element analyses is similar to that described by Qi et al. (2000).

Also, six samples (15CH10, 15CH12a, 15CH12b, 15CH11, 15CH09, and 15SM13) were analyzed in Beijing Geoanalysis Technology Co. Ltd. Their major elements were analyzed using X-ray fluorescence (XRF-1800; SHIMADZU) on fused glasses. Loss on ignition was measured after heating to 1,000°C for 3 h in a muffle furnace. The precision of the XRF analyses is within ±2% for the oxides greater than 0.5 wt.% and within ±5% for the oxides greater than 0.1 wt.%. Trace elements were determined by inductively coupled plasma mass spectrometry (7500; Agilent) after acid digestion of samples in Teflon bombs. The sample powders (about 40 mg) were dissolved in Teflon bombs using a HF + HNO_3 mixture for 48 h at about 190°C. The solution was evaporated to incipient dryness, dissolved by concentrated HNO_3, and evaporated at 150°C to dispel the fluorides. The samples were diluted to about 80 g for analysis after re-dissolving in 30% HNO_3 overnight. An internal standard solution containing the element Rh was used to monitor the signal drift during analysis. Analytical results for USGS standards indicated that the uncertainties for most elements were within 5%.

Zircon Lu–Hf Isotope Analysis

The zircon Lu–Hf isotopic composition analyses were carried out in Beijing GeoAnalysis Co., Ltd. (Beijing, China) using a RESO 193 nm laser-ablation system (produced by Australian Scientific Instruments, Canberra, Australia) and a Neptune Plus MC–ICP–MS (produced by Thermo Fisher Instruments, United States). During the experiment, helium was used as the carrier gas for the ablation material, and the laser beam spot diameter was 40 μm. The internationally accepted standard zircon Plešovice was used as the reference material in this test (Sláma et al., 2008). Detailed analytical procedures are described in Wu et al. (2006). The ^{176}Hf/^{177}Hf value of the standard zircon Plešovice tested in this experiment was 0.282485 ± 0.000006 (2σ), which is consistent with the value of the predecessor (Sláma et al., 2008) within the error range. In the calculation of the ε_{Hf} (t) values, the ^{176}Hf/^{177}Hf and ^{176}Lu/^{177}Hf ratios of present-day chondrite and the depleted mantle were (0.0332, 0.282772) and (0.0384, 0.28325), respectively (Blichert-Toft and Albarède, 1997; Griffin et al., 2000). The two-stage Hf model ages (T_{DM2}) were calculated by adopting ^{176}Lu/^{177}Hf = 0.015 for the average continental crust (Griffin et al., 2002).

RESULTS

Zircon U–Pb Age

Geochronological U–Pb zircon data are summarized in **Supplementary Table SA1** and shown in **Figures 6**, **7**. Zircon grains from samples 15CH09 and 15CH12b from the Chorukhdairon pluton and sample 15SM13 from the quartz porphyry of the Kizilnura suite have been subjected to LA–ICP–MS dating in order to reveal the crystallization ages of the magmas. Zircon crystals are colorless, euhedral to subhedral, and ovoid and tabular in shape. The zircon grains are typically 70–250 μm long, with variable concentrations of Th (465–8,061 ppm) and U (758–9,160 ppm), and high Th/U values of 0.32–1.0. The majority of the zircons show well-developed oscillatory zoning with the lack of clear core-rim structures.

For sample 15CH09, one zircon grain gave an older ^{206}Pb/^{238}U age of 315 ± 6 Ma, and twenty-five analyses gave the ^{206}Pb/^{238}U ages ranging from 303 to 285 Ma, with a weighted mean age of 294 ± 2 Ma (MSWD = 4.3, n = 25) (**Figure 7A**). One zircon analysis from sample 15CH12b yielded an older ^{206}Pb/^{238}U age of 330 ± 6 Ma, and twenty-six analyses gave ^{206}Pb/^{238}U ages ranging from 283 to 301 Ma, with a weighted mean age of 291 ± 2 Ma (MSWD = 4.6, n = 26) (**Figure 7B**), which is identical to that of the zircons from sample 15CH09 within the error. For sample 15SM13, two analyses gave older ^{206}Pb/^{238}U ages (312 ± 7 Ma and 308 ± 5 Ma), and five analyses yielded younger ^{206}Pb/^{238}U ages varying between 273 and 249 Ma, which could reflect zircon inheritance and Pb loss, respectively. Eighteen analyses from 15SM13 yielded ^{206}Pb/^{238}U ages ranging from 293 to 278 Ma, with a weighted mean age of 286 ± 2 Ma (MSWD = 4.6, n = 18) (**Figure 7C**). The weighted mean ages of 294 ± 2 Ma, 291 ± 2 Ma,

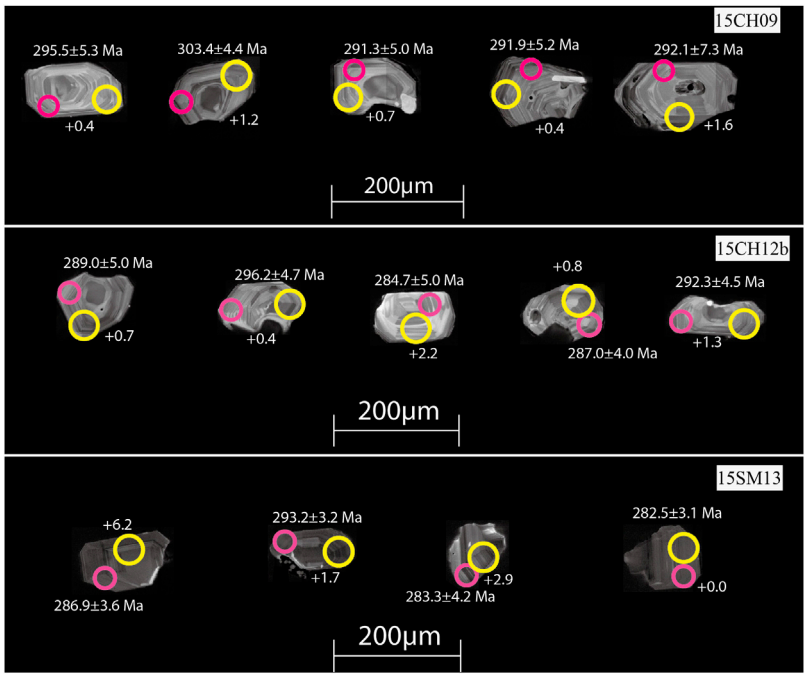

FIGURE 6 | Representative cathodoluminescence images for analyzed zircon grains from the monzogranite (15CH09) and quartz monzonite (15CH12b) of the Chorukhdairon pluton and quartz porphyry (15SM13).

and 286 ± 2 Ma are interpreted here as the magma crystallization ages of rocks.

The aforementioned obtained ages indicate that both the Chorukhdairon pluton and the quartz porphyry were formed in the Early Permian, but the quartz porphyry was emplaced slightly later than the Chorukhdairon pluton, which is consistent with the observed geological relationships in the field.

Major and Trace Elements

Our data, together with those reported by Konopelko et al. (2017) for two samples are used to shape the geochemical variation of the Chorukhdairon pluton (**Supplementary Table SA2**). Based on the TAS classification diagram (**Figure 8A**), the compositions of the rocks from the Chorukhdairon pluton characterize the field of subalkaline series, and the rocks plot further in the fields of monzodiorite, monzonite, quartz monzonite, and granite.

The SiO_2 contents of the samples from the Chorukhdairon pluton and quartz porphyry range from 56.63 to 77.11 wt.%. They are distinguished by high alkalinity, with K_2O + Na_2O contents ranging from 6.65 to 9.26 wt.%. They have high K_2O contents and most of them plot in the shoshonite series field on the K_2O versus SiO_2 diagram (**Figure 8B**). On the K_2O versus Na_2O diagram, all the samples were plotted in the shoshonitic field (**Figure 8C**). The rocks are all metaluminous, with A/CNK of 0.80–0.98, except the late phase leucomonzogranite (A/CNK = 1.07) (**Figure 8D**). On the K_2O + Na_2O–CaO versus SiO_2 diagram, the samples occupy the alkali-calcic and calc-alkalic fields (**Figure 8E**). On the Fe-number versus SiO_2 diagram, one quartz porphyry sample plots in the field of ferroan series, and others fall into the field of magnesian series (**Figure 8F**).

For the rocks of the Chorukhdairon pluton, as the SiO_2 content increases from the first phase to the fourth phase, the contents of Al_2O_3, CaO, $Fe_2O_3^T$, MgO, P_2O_5, and TiO_2 naturally decrease (**Figure 9**), but Na_2O contents show no definite variation trend. The K_2O contents and K_2O/Na_2O ratios in the rocks increase first and then decrease with increasing SiO_2 (**Figures 8B**, **9D**). The maximum K_2O contents (up to 5.90 wt.%) are noted in the quartz monzonites of the main (second) phase (**Figure 8B**).

The samples from the Chorukhdairon pluton and quartz porphyry are characterized by high concentrations of trace elements (e.g., Rb = 57.8–324 ppm; Ba = 327–1,700 ppm; Zr = 80–482 ppm) (**Supplementary Table SA2**). All the samples show similar primitive mantle-normalized trace element patterns characterized by the enrichment of the large ion lithophile elements (LILE, e.g., Rb, Th, U, and K) relative to the high field strength elements (HFSE, e.g., Nb, Ta, P, and Ti) (**Figure 10**). They exhibit moderately to strongly fractionated REE patterns, with $(La/Yb)_N$ ratios of 8.3–20.1. The monzodiorites and quartz monzodiorites of the first phase show weak Eu anomalies, with Eu/Eu* = 0.84–1.00. The quartz monzonite, monzogranite, leucomonzogranite, monzogranitic aplite, and quartz porphyry samples exhibit moderate to strong negative Eu anomalies, with Eu/Eu* ranging from 0.22 to 0.77.

Zircon Lu–Hf Isotopes

In situ zircon Lu–Hf isotopic data are listed in **Supplementary Table SA3** and plotted in **Figure 11**. For all samples, the initial ε_{Hf} (t) and T_{DM}(Hf) values are calculated based on their magma crystallization ages. Twenty spot analyses were obtained for the

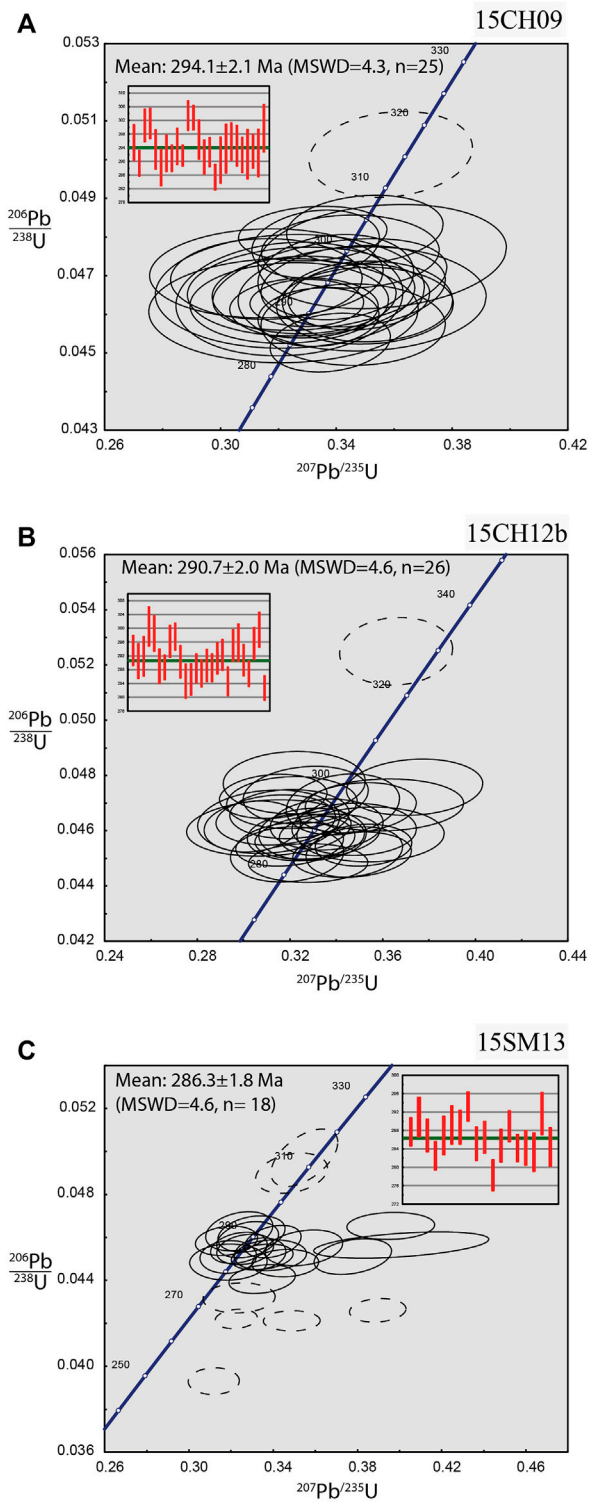

FIGURE 7 | Zircon U–Pb concordia diagrams for monzogranite (15CH09) and quartz monzonite (15CH12b) from the Chorukhdairon pluton and quartz porphyry (15SM13).

zircons from the sample 15CH09 (Chorukhadiron pluton monzogranite), yielding ε_{Hf} (t) values of -0.6 to +1.8, with T_{DM}(Hf) values of 0.85–0.94 Ga. Eighteen spot analyses from the sample 15CH12b (Chorukhadiron pluton quartz monzonite) give ε_{Hf} (t) values ranging from −0.3 to + 2.2, and T_{DM}(Hf) values ranging from 0.80 to 0.94 Ga, which are similar to those of zircons from sample 15CH09. Sixteen zircons were analyzed for sample 15SM13 (quartz porphyry), which yielded a large range of ε_{Hf} (t) values (−0.6 to +6.5) and T_{DM}(Hf) (0.69–0.94 Ga). In **Figure 11**, basically, all analyzed data in this study are located far away from the depleted mantle evolution curve.

DISCUSSION

Petrogenesis

Different hypotheses have been suggested for the origin of potassic magmas worldwide, including 1) partial melting of crustal rocks (Pe-Piper et al., 2009; Campbell et al., 2014), 2) fractional crystallization from mantle-derived basaltic magmas with or without crustal assimilation (Turner et al., 1996; Beermann et al., 2017; Schaarschmidt et al., 2021), and 3) mixing of magma between basic mantle-derived and crustal felsic magmas (Padilha et al., 2019). Consequently, the formation of potassic rocks is a subject of debate, with one significant question, whether such rocks require significant inputs of mantle components. For the mantle-derived LILE- and LREE-enriched shoshonite rocks, they were commonly suggested to form at a late stage of subduction, with geochemical features characteristic of ocean-continent magmatic active zones (LREE enrichment and negative anomalies for Ta, Nb, and Ti) originating from a mantle wedge enriched in incompatible elements due to the previous stage of subduction (Nabatian et al., 2016; Schaarschmidt et al., 2021).

The highly K_2O-enriched characteristics of the four phases of the Chorukhdairon pluton indicate that they are shoshonitic rocks. Their trace elemental composition, as shown in **Figure 12A**, also supports their affinity with shoshonite series rocks. The absence of negative correlation between Nb/La and SiO_2 (**Figure 12B**), combined with the irregular variation of Na_2O contents among the different phases of the Chorukhdairon pluton, suggesting that magma mixing with crustal melts or contamination by crustal materials were not significant during their formation. Their much more depleted zircon Lu–Hf isotopic compositions than those of the Early Permian continental crust-derived rocks such as the granites of the Kyrgysh Complex (Konopelko et al., 2013) (**Figure 11**), also support this inference.

The data for four-phase rocks of the Chorukhdairon pluton generally follow a coherent evolutionary tendency in the Harker diagram (**Figure 9**), and the mafic varieties (monzodiorites) of the Chorukhdairon pluton are characterized by relatively low SiO_2 contents and high contents of MgO (3.54–3.79 wt.%). These,

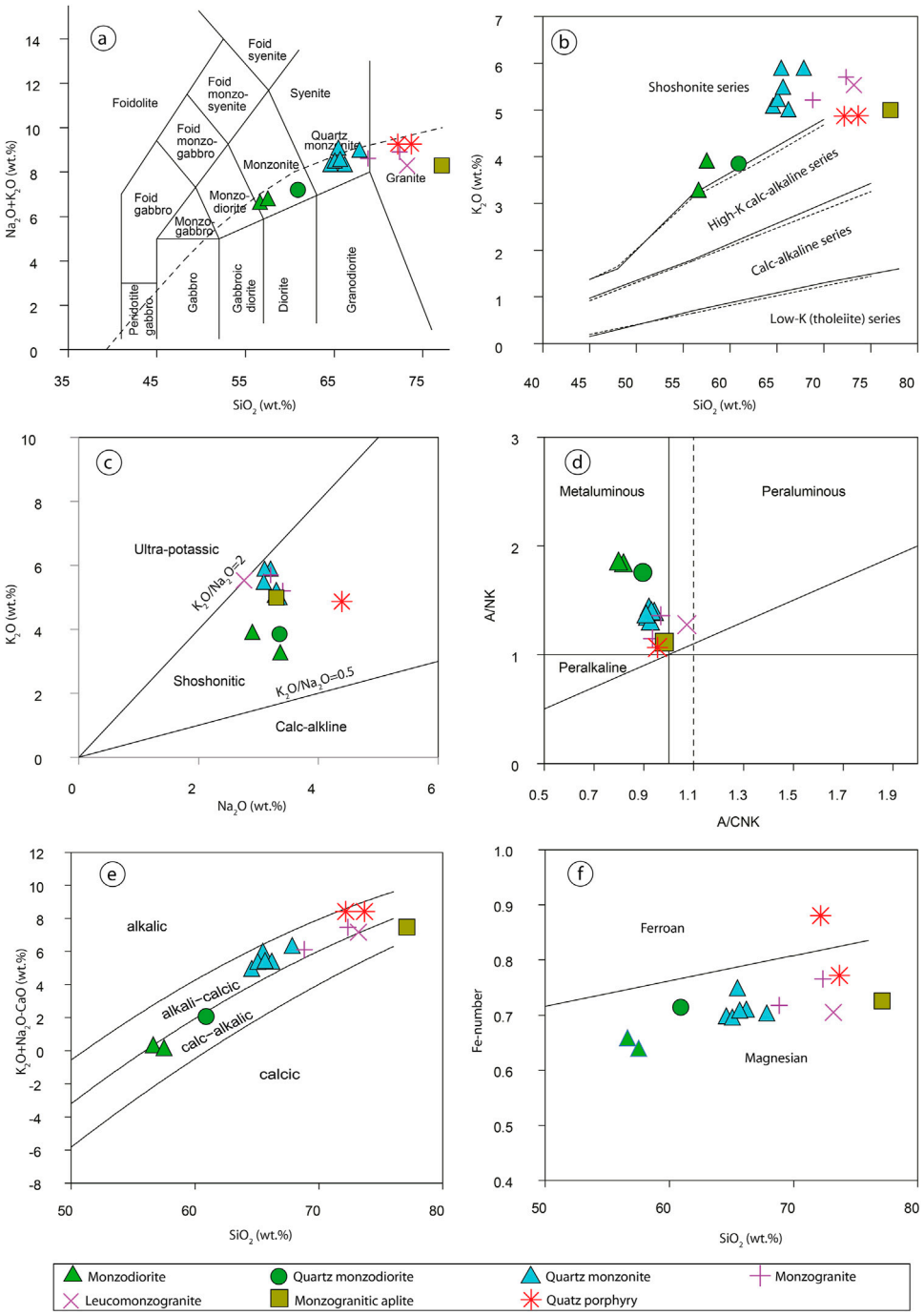

FIGURE 8 | Diagrams of $Na_2O + K_2O$ vs. SiO_2 **(A)** (Le Bas et al., 1986), K_2O vs. SiO_2 **(B)** (Peccerillo and Taylor, 1976), K_2O vs. Na_2O **(C)** (Turner et al., 1996), A/NK—A/CNK **(D)** (Maniar and Piccoli, 1989), $Na_2O + K_2O$–CaO vs. SiO_2 **(E)** (Frost et al., 2001), Fe-number vs. SiO_2 **(F)** (Frost et al., 2001).

combined with their comagmatic nature with the mantle-derived shoshonite series basaltic rocks of the Shurabsai Formation (Mamadjanov, 2004, 2014), indicate that the parental magma of the Chorukhdairon pluton was derived from an enriched mantle source.

The monzodiorites, which are the most mafic varieties of the Chorukhdairon pluton, show shoshonitic geochemical characteristics, suggesting that the high potassic signals of the Chorukhdairon pluton were inherited from their enriched mantle source. The relatively low Mg# values (47–50) and Cr (29.5–47.6 ppm) and Ni (15.9–20.0 ppm) contents of the monzodiorites (**Supplementary Table SA2**), further imply that they were not solidified from primary mantle-derived magmas, but from the evolved melts that experienced significant magma

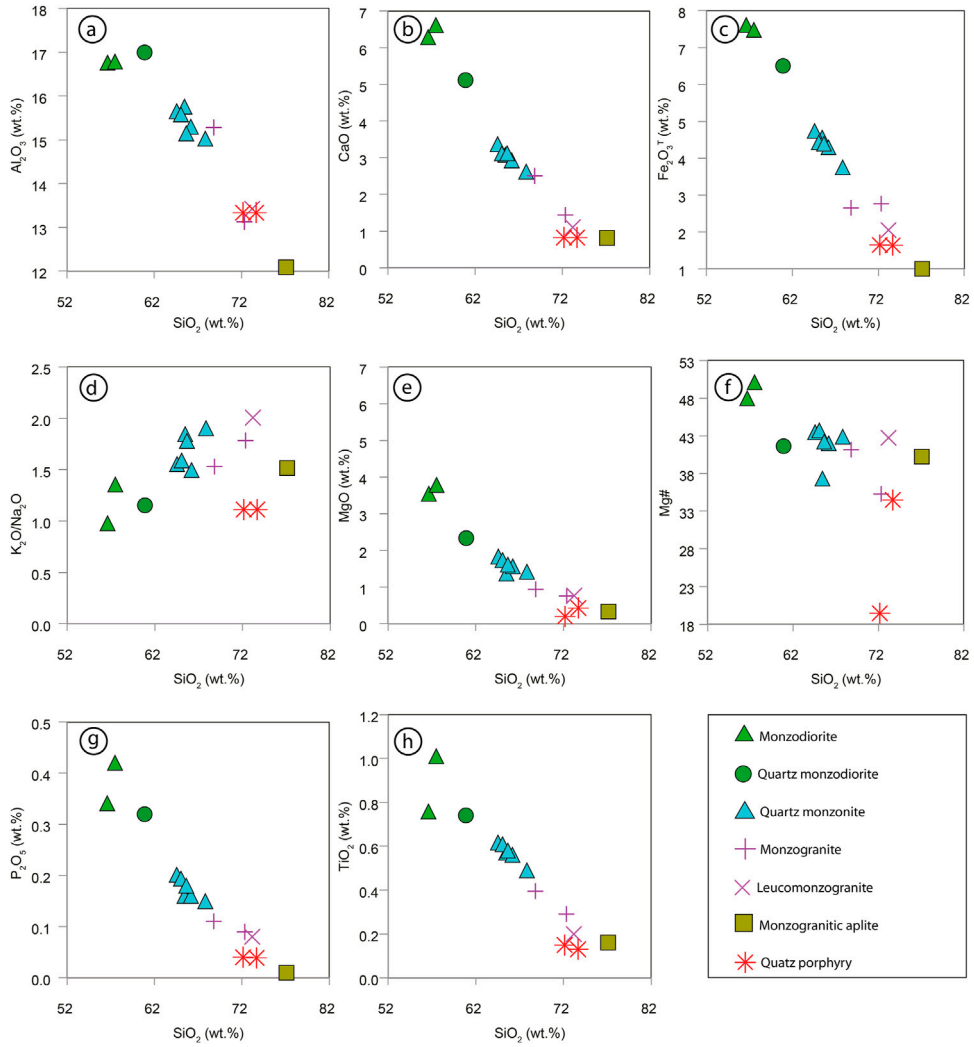

FIGURE 9 | Major element variation diagrams. **(A)** Al_2O_3 vs. SiO_2, **(B)** CaO vs. SiO_2. **(C)** $Fe_2O_3^T$ vs. SiO_2, **(D)** K_2O/Na_2O vs. SiO_2, **(E)** MgO vs. SiO_2, **(F)** Mg# vs. SiO_2, **(G)** P_2O_5 vs. SiO_2, and **(H)** TiO_2 vs. SiO_2.

differentiation. From monzodiorite, through quartz monzodiorite and quartz monzonite, to monzogranite, leucomonzogranite and related monzogranitic aplite, CaO, $Fe_2O_3^T$, MgO, and P_2O_5 and TiO_2 contents gradually decrease with increasing SiO_2 contents (**Figure 9**), consistent with the fractional crystallization of pyroxenes, apatite and accessory Fe–Ti oxides. With magma evolution, Dy/Yb, Al_2O_3, and Eu/Eu* generally decrease (**Figures 9A**, **12C**,D), indicative of fractional crystallization of amphibole and plagioclase. The clear positive correlation between Rb/Sr and Sr (**Figure 12E**) and very low Eu/Eu* ratios in the felsic varieties of the Chorukhdairon pluton suggest that the plagioclase fractionation was very strong. With SiO_2 increasing, K_2O, Rb and Zr increase at first and then decrease (**Figures 8B**, **12F**,G), consistent with the fractional crystallization of biotite and zircon at the late stage of magma evolution. The generally increasing trend of the incompatible elements (e.g., La), and the relatively limited variation of zircon Hf isotopes of the quartz monzonites also support the inference that the fractional crystallization mainly controlled the compositional variation of the different phases of the Chorukhdairon pluton.

The quartz porphyries possess high SiO_2 contents (72.17–73.68 wt.%) and $(K_2O + Na_2O)/CaO$ and FeO^T/MgO ratios, with low A/CNK (~0.95), similar to highly fractionated I-type granites (**Figures 12H,I**). They roughly follow the evolution trend of the Chorukhdairon pluton (**Figures 8A,B**, **9**). This, in combination with their low TiO_2 (0.07–0.08 wt.%), P_2O_5 (~0.04 wt.%), Mg# (19–34), and Eu/Eu* (0.22–0.25) values, suggests the important fractional crystallization of mafic minerals, plagioclase, and accessory minerals in their genesis. Like those from the granodiorite porphyry (314 Ma) of the Kalmakyr porphyry Cu–Au deposit in the Chatkal–Kurama terrane (Zhao et al., 2017) (**Figure 11**), zircons from the quartz porphyry also show a large range of Hf isotopic

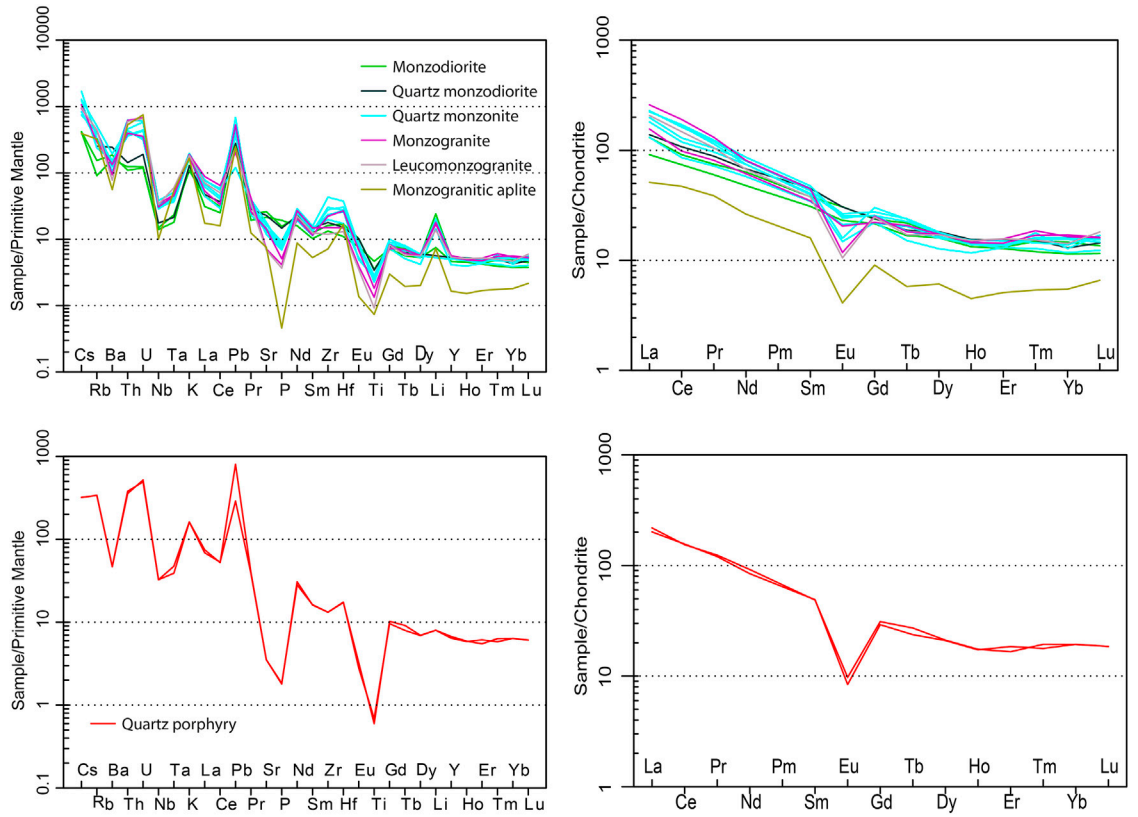

FIGURE 10 | Primitive mantle-normalized trace element spider diagrams and chondrite-normalized REE patterns. Chondrite and primitive mantle normalized values are from Sun and McDonough (1989).

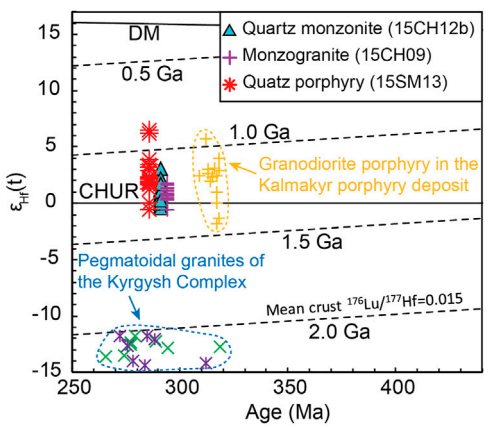

FIGURE 11 | ε_{Hf} (t) vs. zircon U–Pb age diagram. Data of the granodiorite porphyry from the Kalmakyr porphyry Cu–Au deposit and the pegmatoidal granites of the Kyrgysh Complex are from Zhao et al. (2017) and Konopelko et al. (2013), respectively.

compositions, with ε_{Hf} (t) values ranging from −0.6 to +6.5, indicative of the involvement of at least two components in their generation. Considering their relatively juvenile Hf signals and higher zircon saturation temperatures (~770°C), we suggest that their parental magma could be the product of mixing of different batches of mantle-derived magmas or magmas derived from the mantle and juvenile lower crust.

Tectonic Setting of Magma Generation

Shoshonitic magmatism was commonly considered to form in an oceanic subduction (continental arc or oceanic arc) or post-collisional setting (Stern et al., 1988; Turner et al., 1996; Nabatian et al., 2016; Padilha et al., 2019; Casetta et al., 2021; Schaarschmidt et al., 2021). In addition, some researchers also link the generation of shoshonitic rocks to continental subduction (Campbell et al., 2014).

In the history of geological and geodynamic development of the Chatkal–Kurama, Late Paleozoic (C_2-P) stage occupies a special place. In the Late Paleozoic, the zone was distinguished by strong magmatic and metallogenic processes. The evolution of Late Paleozoic magmatism proceeded naturally at the early stages of development. Calc-alkaline rocks appeared first, and later, subalkaline and alkaline igneous rocks occurred, which is the characteristic of active continental margins (Mamadjanov, 2014). A characteristic feature of Late Paleozoic magmatism in the studied zone is the formation of polyfacial, complexly constructed volcano-plutonic associations, accompanied by the industrial and unique deposits of gold, silver, iron, copper, base metals, molybdenum, and tungsten. (Mamadjanov, 2014). Based

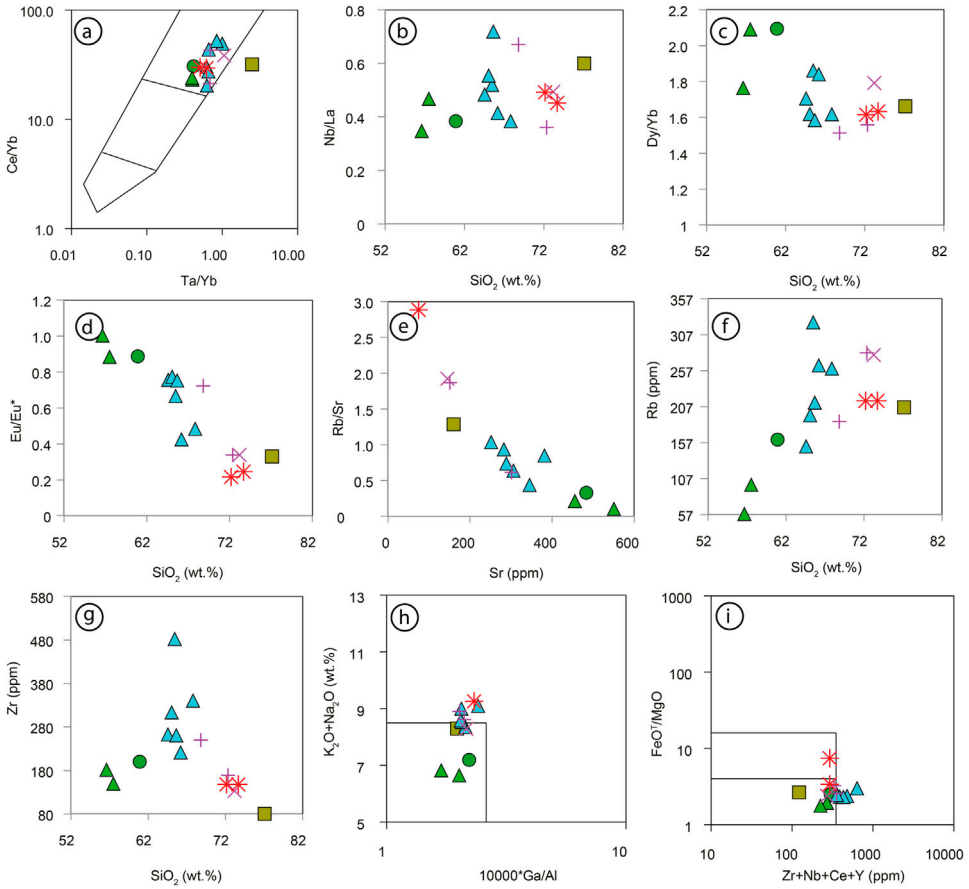

FIGURE 12 | Diagrams of Ce/Yb vs. Ta/Yb **(A)** (Pearce, 1982), Nb/La vs. SiO_2 **(B)**, Dy/Yb vs. SiO_2 **(C)**, Eu/Eu* vs. SiO_2 **(D)**, Rb/Sr vs. Sr **(E)**, Rb vs. SiO_2 **(F),** and Zr vs. SiO_2 **(G)**, and geochemical discrimination diagrams of K_2O + Na_2O vs. 10000*Ga/Al **(H)** and FeOT/MgO vs. Zr + Nb + Ce + Y) **(I)** for A-type granites (Whalen et al., 1987). Symbols are shown in **Figure 8**.

on the changes in the magma series, some researchers suggested that the Late Paleozoic igneous formations in the Chatkal–Kurama zone are associated with oceanic subduction (Middle Carboniferous to late stage of the Late Carboniferous), late subduction-collisional (end of the Late Carboniferous to Early Permian), and post-collisional (Middle Permian) stages during the geological development of the continental-marginal Kyzylkum–Kurama volcanic belt (Mamadjanov, 2014; Dolgopolova et al., 2017).

From the Middle Carboniferous, on the southern (in modern coordinates) margin of the Kazakhstan paleocontinent, active subduction processes restarted. As a result of the subduction of the Turkestan oceanic crust, the extensive magmatic activity began under the southern margin of the Kazakhstan paleocontinent, leading to the generation of the 340–335 Ma gabbroic and granodioritic rocks in the Almalyk Cu–Au orefield and its adjacent area (Cheng et al., 2018a; Cheng et al., 2018b), and subsequent formation of the Chatkal–Kurama volcano-plutonic belt. From ~340 to 286 Ma, the magmatism was continuous with a magmatic flare-up at ~310 Ma (**Figure 13**), suggesting that magmatic rocks generated during this period could form in a similar tectonic setting. The rocks of this study are all characterized by the clear enrichment of LILE (e.g., Cs, Rb, and K) and depletion of HFSE (e.g., Nb, Ta, and Ti), and show Rb and Y + Nb contents similar to those of typical volcanic arc granites (Pearce et al. (1984), consistent with their formation in a subduction setting. By reviewing structural relations and petrochemical, geochronological, biostratigraphic, and paleomagnetic data on the Altaids, Xiao et al. (2015) suggested that the South Tianshan (or Turkestan) Ocean could have not been closed in the Early Permian. Recent studies on field relations, geochronology, and geochemistry of the accretionary complex in the Kyrgyz and Chinese South Tianshan (Sang et al., 2017; Sang et al., 2018; Abuduxun et al., 2021) also implied that the subduction of the South Tianshan (or Turkestan) oceanic slab was still active in the Late Carboniferous to Early Permian. Thus, the shoshonitic rocks and related dykes in this study probably formed in an oceanic subduction setting.

Implications and Speculations on the Geodynamics

The accretionary orogenic belt is characterized by long-time oceanic subduction and accretion processes, accompanied by

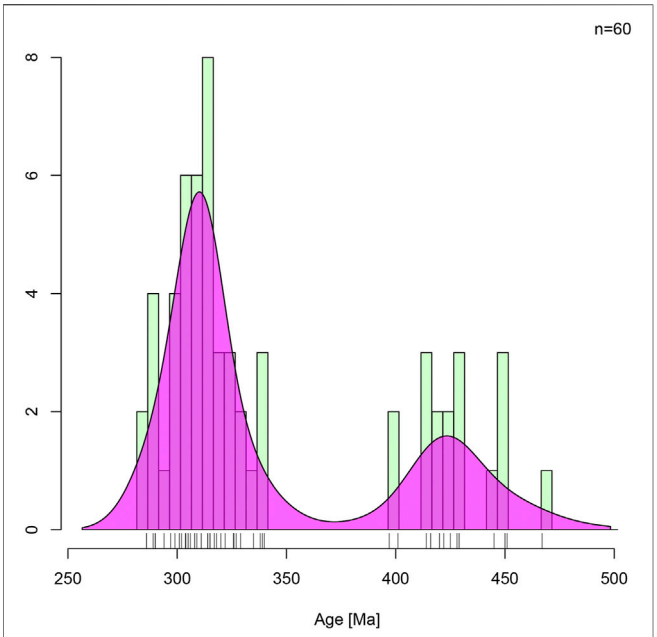

FIGURE 13 | Histograms of U–Pb ages of the Paleozoic magmatic rocks in the Chatkal–Kurama terrane. Data sources: (Seltmann et al., 2011; Mirkamalov et al., 2012; Alexeiev et al., 2016; Dolgopolova et al., 2017; Konopelko et al., 2017; Zhao et al., 2017; Cheng et al., 2018a; Cheng et al., 2018b; Zu et al., 2019) and this study.

complex slab geodynamic processes (e.g., ridge subduction, slab roll back, flat subduction, and slab break-off) and prolonged magmatism. The Chatkal–Kurama terrane, which is an important part of the Middle Tianshan belt that is traditionally considered a continental magmatic arc built on an ancient basement, was constructed predominately during the northward subduction of the Turkestan Ocean, a southern branch of the Paleo-Asian Ocean, during the Paleozoic. Thus, it is the key area to understand the Paleozoic slab dynamics that occurred in the southwest of the Altaids as well as the late evolution history of the Paleo-Asian Ocean.

Previous studies have reported Early Paleozoic arc-related magmatic rocks in the Chatkal–Kurama terrane, including granite, granodiorite and granodioritic, and syenitic porphyries, which possess magma crystallization ages ranging from ~450 to ~420 Ma and some of which show shoshonitic geochemical characteristics (Alexeiev et al., 2016; Dolgopolova et al., 2017).

In the Early Devonian, typical arc magmatic products in the Chatkal–Kurama terrane were mainly monzonite, granite, microgranite-porphyry, and micropegmatite (Seltmann et al., 2011; Dolgopolova et al., 2017). They were emplaced at 416–397 Ma, and mostly display a shoshonitic affinity. However, after that, the Chatkal–Kurama terrane experienced a period (over 50 Ma) of magmatic quiescence (**Figure 13**). Thus, an issue arises, what was the driven force that caused a magmatic lull by that time. Considering that the major ocean (Turkestan Ocean in this case) was not closed, this episode of lull in magmatism in other orogenic belts is often linked to the flat (low-angle (<10°) or sub-horizontal) subduction of the oceanic slab (Haschke et al., 2002; Zhang et al., 2017; Yan et al., 2020), which would result in weakening or termination of arc magma activity because of the gradual disappearance of the hot mantle

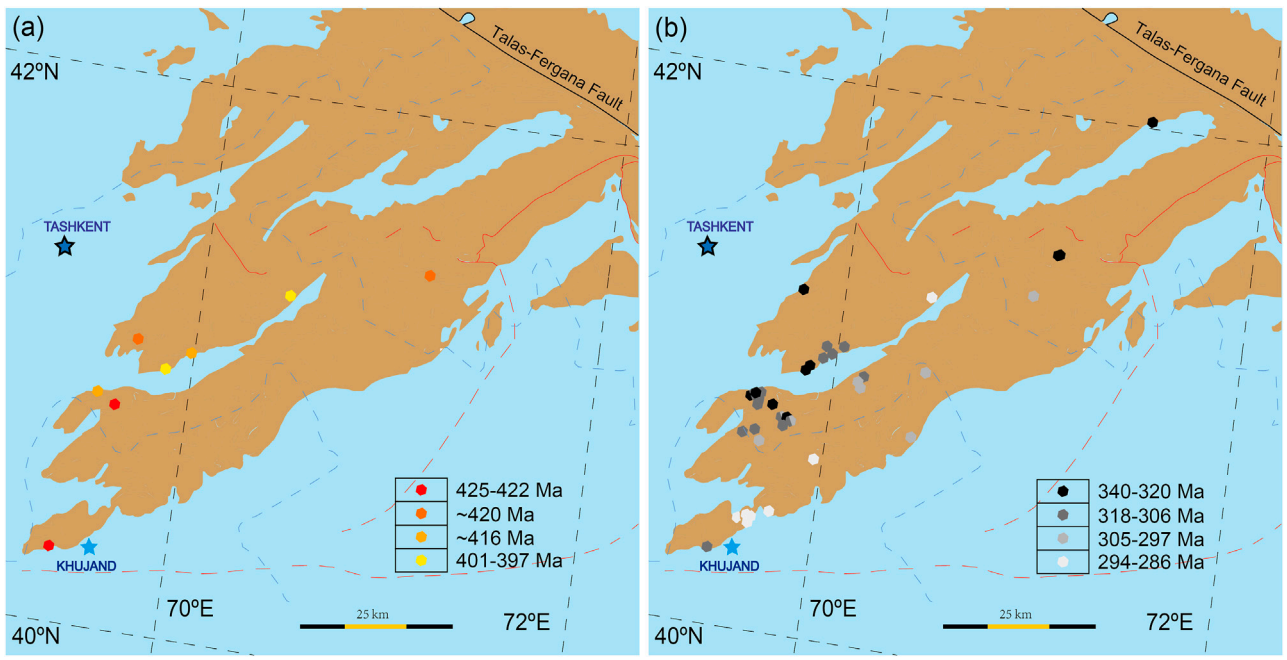

FIGURE 14 | Temporal–spatial distribution diagram of the Paleozoic magmatism in the Chatkal–Kurama terrane of the Middle Tianshan. Data source is the same as that of **Figure 2**.

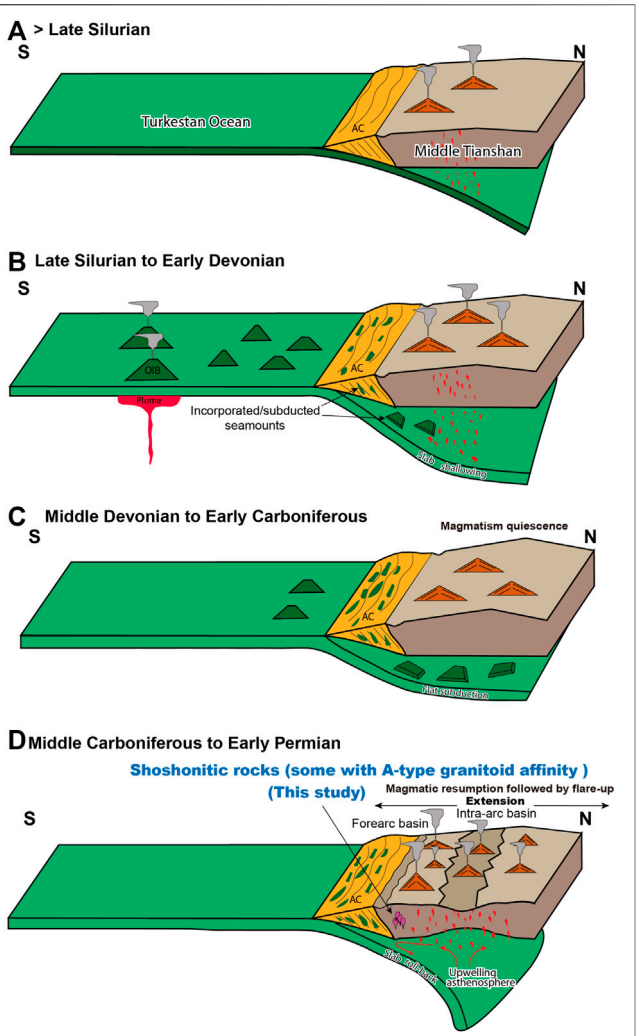

FIGURE 15 | Schematic cartoon illustrating the Paleozoic tectonic evolution of the Chatkal–Kurama terrane in the Middle Tianshan. **(A)** Pre-Late Silurian. Normal subduction of the Turkestan oceanic slab; **(B)** Late Silurian to Early Devonian. Shallowing of subducted slab due to the seamount subduction/accretion, with arc magmatism migration toward the interior of the arc; **(C)** Middle Devonian to Early Carboniferous. Flat subduction with the occurrence of magmatic quiescence; **(D)** Middle Carboniferous to Early Permian. Slab roll-back and the resulted arc magmatism migration, magmatic flare-up and extensional tectonics in the Chatkal–Kurama terrane.

wedge due to the flattening of subducted slab. Previous researchers have demonstrated that flat subduction can be induced by the relative buoyancy of subducted oceanic plateaus/seamounts/aseismic ridges, overthrusting of the overriding plate, or slab suction forces (van Hunen et al., 2004; Yan et al., 2020). We noticed that Late Silurian to Middle Devonian OIB-type rocks and related limestone have been reported in the Kyrgyz South Tianshan accretionary complexes, which indicated the accretion of one or several seamount chains of the Turkestan (or South Tianshan) Ocean to the Middle Tianshan during Late Silurian to Devonian (Safonova et al., 2016; Sang et al., 2020). Such a seamount chain accretion is consistent with the expected results during (or after) the flat subduction caused by the subduction of seamount-bearing thick and buoyant oceanic crust. In fact, the exhumation of subducted seamounts, which have been transformed to blueschist-and eclogite-facies (OIB-/E-MORB-type mafic) rocks that formed through high-pressure metamorphism at ~344 Ma, have been discovered in the South Tianshan of the Akeyazi area (Gao and Klemd, 2003). From 425 Ma to 397 Ma, magmatism propagated toward the interior of the Chatkal–Kurama terrane (**Figure 14A**), coinciding with the proceeding of flat subduction.

In the Middle Devonian, the Chatkal–Kurama terrane underwent uplift and erosion (Dolgopolova et al., 2017; Konopelko et al., 2017), also consistent with the resulted compressional regime in the overriding plate following the occurrence of flat subduction (Espurt et al., 2008; Yan et al., 2020). Unlike the situation in the Late Silurian–Early Carboniferous at which time the granitoids generally show high HREE contents (Alexeiev et al., 2016; Dolgopolova et al., 2017; Konopelko et al., 2017), from 338 Ma after the restarting of arc magmatism following the end of magmatic quiescence, the HREE-depleted ore-bearing porphyries and related porphyry Cu–Au deposits successively occurred, such as those in the Almalyk orefield in the southwestern Chatkal–Kurama terrane (Cheng et al., 2018a). The occurrence of these types of rocks and related deposits are consistent with the existence of a thicker crust, which might result from the former flat subduction-induced compression (Yan et al., 2020). Thus, the flat-slab subduction that was induced by the subduction/accretion of seamounts probably occurred beneath the Middle Tianshan during the Middle Devonian to Early Carboniferous.

The occurrence of ~340 Ma arc-related gabbros in the Akcha and Beleuti areas of the Chatkal–Kurama terrane indicates the subduction of the Turkestan oceanic slab resumed. Following that, continuous arc magmatism occurred with a peak at ~310 Ma (**Figure 13**). As shown in **Figure 14B**, the arc magmatism shows a rough migration toward the southeast of the Chatkal–Kurama terrane, resulting in the generation of the 294–286 Ma shoshonitic intrusive magmatism and rhyolitic magmatism along the southeastern margin of the Chatkal–Kurama terrane. We suggest that this magmatic migration indicates the slab roll-back following the end of flat subduction, which could cause retreating of the subduction zone and significant extension of the overlying lithosphere (Kusky et al., 2014). As shown in **Figures 12H,I**, some rocks of the Chorukhdairon pluton [e.g., quartz monzonites with high zircon saturation temperatures (up to ~860°C)] share an affinity with A-type granitoids, which agrees with the extension related to the slab roll-back. Our conclusion on the slab roll-back model and generation of A-type granitoids in syn-subduction extensional environment is consistent with the interpretation for the Permian A-type granitoids of the Chinese South Tianshan (Abuduxun et al., 2022). In addition, the occurrence of 320–299 Ma mafic to felsic dykes in the Chatkal–Kurama terrane (Dolgopolova et al., 2017; Cheng et al., 2018a) also supports the view of slab roll-back-induced extension of the upper plate. As documented by Burtman (2015), in the Tianshan, Permian volcanic and volcanogenic sediments overlying the Late Carboniferous and older rocks often fill graben structures,

which is typical for the Chatkal–Kurama area of the Western Tianshan (with a high thickness of this type of deposit, up to 4 km), consistent with the development of arc-related extensional basin in the Chatkal–Kurama terrane. Other studies also suggested that the Permian shoshonitic volcanic rocks in some parts of the Chatakal–Kurama terrane formed within volcanic troughs and volcanotectonic depressions (Mamadjanov, 2004; Mamadjanov, 2014), and alkaline-basaltic volcanic rocks of trachybasalt–leucite–trachyte composition within the Ugam-Daubob graben (Mamadjanov, 2013). The widespread Permian potassium alkaline magmatism in the Chatkal–Kurama terrane is also in line with the occurrence of extensional zones (Mamadjanov, 2014; Burtman, 2015). Similar extensional faulted basins were also identified to occur in Chinese Central Tianshan–Yili arc and the South Tianshan belt during the Early Permian (Liu et al., 2013; Li et al., 2015). Therefore, the southeastward slab roll-back could occur beneath the Middle Tianshan during the Middle Carboniferous to the Early Permian, which was responsible for the southeastward magmatism migration and magmatic flare-up, with formation of some extensional arc-related basins including forearc and intra-arc basins in the Chatkal–Kurama terrane (**Figure 15**).

Overall, the Early Permian Chorukhdairon intrusive rocks and quartz porphyry and other Paleozoic magmatic rocks in the Chatkal–Kurama terrane recorded geodynamic processes from flat subduction to slab roll-back at the southwestern Altaids.

CONCLUSION

The Chorukhdairon pluton is mainly composed of four phases: monzodiorite and quartz monzodiorite (first phase), quartz monzonite (second and main phase), monzogranite (third phase) and leucomonzogranite (final phase). The monzogranite–quartz monzonite of the Chorukhdairon pluton and quartz porphyry were emplaced at 294–291 Ma and 286 Ma, respectively. The Chorukhdairon pluton was produced by the partial melting of enriched mantle, followed by the fractional crystallization of pyroxenes, amphibole, plagioclase, biotite and accessory Fe–Ti oxides, apatite, and zircon. The quartz porphyry was generated by mixing the different batches of mantle-derived magmas or magmas derived from the mantle and juvenile lower crust, followed by strong fractional crystallization. The Chorukhdairon pluton and related quartz porphyry probably formed in an oceanic subduction setting. Furthermore, the flat-slab subduction probably occurred beneath the Middle Tianshan during the Middle Devonian to Early Carboniferous. Following the end of the flat subduction, southeastward slab roll-back occurred during the Middle Carboniferous to the Early Permian. The late slab roll-back led to the southeastward arc magmatism migration and magmatic flare-up in the Chatkal–Kurama terrane, western Tianshan, and contributed significantly to the crustal growth at the southwestern Altaids.

DATA AVAILABILITY STATEMENT

The original contributions presented in this study are included in the article/**Supplementary Material**, further inquiries can be directed to the corresponding authors.

ETHICS STATEMENT

Written informed consent was obtained from the individual(s) for the publication of any identifiable images or data included in this article.

AUTHOR CONTRIBUTIONS

This manuscript was designed and written by HY, MS, WX, and GK. The initial data were provided by HY and YM. Other co-authors attended the field work and revision of the manuscript.

FUNDING

This study was financially supported by the Open Project of Key Laboratory, Xinjiang Uygur Autonomous Region (2020D04041), the National Natural Science Foundation of China (41888101, 42072269), the Science and Technology Major Project of Xinjiang Uygur Autonomous Region, China (2021A03001), the CAS "Light of West China" Program (2018-XBYJRC-003), and the Project of China–Pakistan Joint Research Center on Earth Sciences, CAS (131551KYSB20200021). This is a contribution to IGCP 662 and IGCP 710.

ACKNOWLEDGMENTS

The authors are grateful to two reviewers for their careful reviews, which greatly improved the manuscript. They also want to thank Professor Hanlin Chen for editorial handling.

SUPPLEMENTARY MATERIAL

The Supplementary Material for this article can be found online at: https://www.frontiersin.org/articles/10.3389/feart.2022.893751/full#supplementary-material

REFERENCES

Abuduxun, N., Xiao, W., Windley, B. F., Chen, Y., Huang, P., Sang, M., et al. (2021). Terminal Suturing between the Tarim Craton and the Yili-Central Tianshan Arc: Insights from Mélange-Ocean Plate Stratigraphy, Detrital Zircon Ages, and Provenance of the South Tianshan Accretionary Complex. *Tectonics* 40, e2021TC006705. doi:10.1029/2021TC006705

Abuduxun, N., Xiao, W., Windley, B. F., Huang, P., Yang, H., Gan, J., et al. (2022). Early Permian Syn-Subduction Extension in the South Tianshan (NW China): Insights from A-type Granitoids in the Southern Altaids. *Front. Earth Sci.* 9, 831677. doi:10.3389/feart.2021.831677

Alexeiev, D. V., Kröner, A., Hegner, E., Rojas-Agramonte, Y., Biske, Y. S., Wong, J., et al. (2016). Middle to Late Ordovician Arc System in the Kyrgyz Middle Tianshan: From Arc-Continent Collision to Subsequent Evolution of a Palaeozoic continental Margin. *Gondwana Res.* 39, 261–291. doi:10.1016/j.gr.2016.02.003

Le Bas, M. J., Maitre, R. W. L., Streckeisen, A., Zanettin, B., and Rocks, I. S. o. t. S. o. I. (1986). A Chemical Classification of Volcanic Rocks Based on the Total Alkali-Silica Diagram. *J. Petrology* 27, 745–750. doi:10.1093/petrology/27.3.745

Baratov, R. B. (1976). *Subdivision of Stratified and Intrusive Rocks of Tajikistan*. Dushanbe: Donish, 269. (in Russian).

Beermann, O., Holtz, F., and Duesterhoeft, E. (2017). Magma Storage Conditions and Differentiation of the Mafic Lower Pollara Volcanics, Salina Island, Aeolian Islands, Italy: Implications for the Formation Conditions of Shoshonites and Potassic Rocks. *Contrib. Mineral. Petrol.* 172, 1–21. doi:10.1007/s00410-017-1363-z

Biske, Y. S., and Seltmann, R. (2010). Paleozoic Tian-Shan as a Transitional Region between the Rheic and Urals-Turkestan Oceans. *Gondwana Res.* 17, 602–613. doi:10.1016/jgr.2009.11.01410.1016/j.gr.2009.11.014

Blichert-Toft, J., and Albarède, F. (1997). The Lu-Hf Isotope Geochemistry of Chondrites and the Evolution of the Mantle-Crust System. *Earth Planet. Sci. Lett.* 148, 243–258. doi:10.1016/S0012-821X(97)00040-X

Burtman, V. S. (2015). Tectonics and Geodynamics of the Tian Shan in the Middle and Late Paleozoic. *Geotecton.* 49, 302–319. doi:10.1134/s0016852115040020

Burtman, V. S. (2010). Tien Shan, Pamir, and Tibet: History and Geodynamics of Phanerozoic Oceanic Basins. *Geotecton.* 44, 388–404. doi:10.1134/s001685211005002x

Burtman, V. (2006). The Tien Shan Early Paleozoic Tectonics and Geodynamics. *Russ. J. Earth Sci.* 8, 1–23. doi:10.2205/2006es000202

Campbell, I. H., Stepanov, A. S., Liang, H.-Y., Allen, C. M., Norman, M. D., Zhang, Y.-Q., et al. (2014). The Origin of Shoshonites: New Insights from the Tertiary High-Potassium Intrusions of Eastern Tibet. *Contrib. Mineral. Petrol.* 167, 1–22. doi:10.1007/s00410-014-0983-9

Casetta, F., Ickert, R. B., Mark, D. F., Giacomoni, P. P., Bonadiman, C., Ntaflos, T., et al. (2021). The Variscan Subduction Inheritance in the Southern Alps Sub-Continental Lithospheric Mantle: Clues from the Middle Triassic Shoshonitic Magmatism of the Dolomites (NE Italy). *Lithos* 380-381, 105856. doi:10.1016/j.lithos.2020.105856

Cawood, P. A., Kröner, A., Collins, W. J., Kusky, T. M., Mooney, W. D., and Windley, B. F. (2009). Accretionary Orogens through Earth History. *Geol. Soc. Lond. Spec. Publications* 318, 1–36. doi:10.1144/SP318.1

Chapman, J. B., and Ducea, M. N. (2019). The Role of Arc Migration in Cordilleran Orogenic Cyclicity. *Geology* 47, 627–631. doi:10.1130/G46117.1

Cheng, Z., Zhang, Z., Chai, F., Hou, T., Santosh, M., Turesebekov, A., et al. (2018a). Carboniferous Porphyry Cu-Au Deposits in the Almalyk orefield, Uzbekistan: the Sarycheku and Kalmakyr Examples. *Int. Geology. Rev.* 60, 1–20. doi:10.1080/00206814.2017.1309996

Cheng, Z., Zhang, Z., Turesebekov, A., Nurtaev, B. S., Xu, L., and Santosh, M. (2018b). Petrogenesis of Gabbroic Intrusions in the Valerianov-Beltau-Kurama Magmatic Arc, Uzbekistan: The Role of Arc Maturity Controlling the Generation of Giant Porphyry Cu-Au Deposits. *Lithos* 320-321, 75–92. doi:10.1016/j.lithos.2018.08.039

Condie, K. C. (2007). Accretionary Orogens in Space and Time. *Mem. Geol. Soc. Am. Bull.* 200, 145–158. doi:10.1130/2007.1200(0910.1130/2007.1200(09)

DeCelles, P. G., Ducea, M. N., Kapp, P., and Zandt, G. (2009). Cyclicity in Cordilleran Orogenic Systems. *Nat. Geosci* 2, 251–257. doi:10.1038/NGEO469

Dolgopolova, A., Seltmann, R., Konopelko, D., Biske, Y. S., Shatov, V., Armstrong, R., et al. (2017). Geodynamic Evolution of the Western Tien Shan, Uzbekistan: Insights from U-Pb SHRIMP Geochronology and Sr-Nd-Pb-Hf Isotope Mapping of Granitoids. *Gondwana Res.* 47, 76–109. doi:10.1016/j.gr.2016.10.022

Espurt, N., Funiciello, F., Martinod, J., Guillaume, B., Regard, V., Faccenna, C., et al. (2008). Flat Subduction Dynamics and Deformation of the South American Plate: Insights from Analog Modeling. *Tectonics* 27, a–n. doi:10.1029/2007TC002175

Ferrari, L., Valencia-Moreno, M., and Bryan, S. E. (2007). Magmatism and Tectonics of the Sierra Madre Occidental and its Relation with the Evolution of the Western Margin of North America. *Spec. Pap. Geol. Soc. Am. Bull.* 422, 1–39. doi:10.1130/2007.2422(0110.1130/2007.2422(01)

Frost, B. R., Barnes, C. G., Collins, W. J., Arculus, R. J., Ellis, D. J., and Frost, C. D. (2001). A Geochemical Classification for Granitic Rocks. *J. Petrol.* 42, 2033–2048. doi:10.1093/petrology/42.11.2033

Gao, J., and Klemd, R. (2003). Formation of HP-LT Rocks and Their Tectonic Implications in the Western Tianshan Orogen, NW China: Geochemical and Age Constraints. *Lithos* 66, 1–22. doi:10.1016/S0024-4937(02)00153-6

Glorie, S., De Grave, J., Buslov, M. M., Zhimulev, F. I., Stockli, D. F., Batalev, V. Y., et al. (2011). Tectonic History of the Kyrgyz South Tien Shan (Atbashi-Inylchek) Suture Zone: The Role of Inherited Structures during Deformation-Propagation. *Tectonics* 30, a–n. doi:10.1029/2011tc002949

Griffin, W. L., Pearson, N. J., Belousova, E., Jackson, S. E., van Achterbergh, E., O'Reilly, S. Y., et al. (2000). The Hf Isotope Composition of Cratonic Mantle: LAM-MC-ICPMS Analysis of Zircon Megacrysts in Kimberlites. *Geochim. Cosmochim. Acta.* 64, 133–147. doi:10.1016/S0016-7037(99)00343-9

Griffin, W. L., Wang, X., Jackson, S. E., Pearson, N. J., O'Reilly, S. Y., Xu, X., et al. (2002). Zircon Chemistry and Magma Mixing, SE China: *In-Situ* Analysis of Hf Isotopes, Tonglu and Pingtan Igneous Complexes. *Lithos* 61, 237–269. doi:10.1016/S0024-4937(02)00082-8

Guivel, C., Morata, D., Pelleter, E., Espinoza, F., Maury, R. C., Lagabrielle, Y., et al. (2006). Miocene to Late Quaternary Patagonian Basalts (46-47°S): Geochronometric and Geochemical Evidence for Slab Tearing Due to Active Spreading ridge Subduction. *J. Volcanology Geothermal Res.* 149, 346–370. doi:10.1016/j.jvolgeores.2005.09.002

Haschke, M. R., Scheuber, E., Gunther, A., and Reutter, K.-J. (2002). Evolutionary Cycles during the Andean Orogeny: Repeated Slab Breakoff and Flat Subduction? *Terra Nova* 14, 49–55. doi:10.1046/j.1365-3121.2002.00387.x

Ivanov, K. S., Mikolaichuk, A. V., Puchkov, V. N., Erokhin, Y. V., and Khristov, E. V. (2002). The Mid-tien-Shan Ophiolites: Structural Position and Age. *Geol. Geofiz.* 43, 1093–1098. doi:10.1023/a:1014797105633

Jahn, B.-M. (2004). The Central Asian Orogenic Belt and Growth of the continental Crust in the Phanerozoic. *Geol. Soc. Lond. Spec. Publications* 226, 73–100. doi:10.1144/GSL.SP.2004.226.01.05

Käßner, A., Ratschbacher, L., Pfänder, J. A., Hacker, B. R., Zack, G., Sonntag, B.-L., et al. (2017). Proterozoic-Mesozoic History of the Central Asian Orogenic belt in the Tajik and Southwestern Kyrgyz Tian Shan: U-Pb,40Ar/39Ar, and Fission-Track Geochronology and Geochemistry of Granitoids. *Geol. Soc. America Bull.* 129, 281–303. doi:10.1130/b31466.1

Konopelko, D., Seltmann, R., Apayarov, F., Belousova, E., Izokh, A., and Lepekhina, E. (2013). U-Pb-Hf Zircon Study of Two Mylonitic Granite Complexes in the Talas-Fergana Fault Zone, Kyrgyzstan, and Ar-Ar Age of Deformations along the Fault. *J. Asian Earth Sci.* 73, 334–346. doi:10.1016/j.jseaes.2013.04.046

Konopelko, D., Seltmann, R., Mamadjanov, Y., Romer, R. L., Rojas-Agramonte, Y., Jeffries, T., et al. (2017). A Geotraverse across Two Paleo-Subduction Zones in Tien Shan, Tajikistan. *Gondwana Res.* 47, 110–130. doi:10.1016/j.gr.2016.09.010

Kröner, A., Alexeiev, D. V., Kovach, V. P., Rojas-Agramonte, Y., Tretyakov, A. A., Mikolaichuk, A. V., et al. (2017). Zircon Ages, Geochemistry and Nd Isotopic Systematics for the Palaeoproterozoic 2.3-1.8 Ga Kuilyu Complex, East Kyrgyzstan - the Oldest continental Basement Fragment in the Tianshan Orogenic belt. *J. Asian Earth Sci.* 135, 122–135. doi:10.1016/j.jseaes.2016.12.022

Kusky, T. M., Windley, B. F., Wang, L., Wang, Z., Li, X., and Zhu, P. (2014). Flat Slab Subduction, Trench Suction, and Craton Destruction: Comparison of the North China, Wyoming, and Brazilian Cratons. *Tectonophysics* 630, 208–221. doi:10.1016/j.tecto.2014.05.028

Li, D., He, D., Tang, Y., Wu, X., Lian, Y., and Yang, Y. (2015). Dynamic Processes from Plate Subduction to Intracontinental Deformation: Insights from the Tectono-Sedimentary Evolution of the Zhaosu-Tekesi Depression in the Southwestern Chinese Tianshan. *J. Asian Earth Sci.* 113, 728–747. doi:10.1016/j.jseaes.2015.09.007

Liu, D., Jolivet, M., Yang, W., Zhang, Z., Cheng, F., Zhu, B., et al. (2013). Latest Paleozoic-Early Mesozoic basin-range Interactions in South Tian Shan (Northwest China) and Their Tectonic Significance: Constraints from

Detrital Zircon U-Pb Ages. *Tectonophysics* 599, 197–213. doi:10.1016/j.tecto.2013.04.018

Mamadjanov, Y. (2014). "Absarokite-shoshonite-latite Series of the Tashkesken-Samgar Volcanic Structure of the Chatkal-Kurama Zone of the Middle Tien Shan," in *Proceedings of the Academy of Sciences of the Republic of Tajikistan* (Dushanbe: Department of Physical and Mathematical, Chemical, Geological and Technical Sciences), 156, 88–99. (in Russian with English abstract).

Mamadjanov, Y. (2004). *Geodynamics and Metallogeny of Shoshonite-Latite Magmatism of the Middle Tien Shan*. Dushanbe: Devashtitch Publishing House, 192. p (in Russian).

Mamadjanov, Y. (2013). Geodynamics, Mineralization and Geoecological Problems of the Tien Shan. *Bishkek: Ilim*, 156–163. (in Russian).

Mamadjanov, Y. (1995). *Petrology and Geochemistry of the Shoshonite-Latite Association of the Kurama Zone*. Dushanbe: Tajikistan Institute of Geology, 24. p (in Russian).

Mamadjanov, Y., and Tajibaev, G. T. (1987). Shoshonites of the Karamazar (Middle Tien Shan). *Trans. Sci. Acad. Tajikistan* 30, 116–119. (in Russian).

Maniar, P. D., and Piccoli, P. M. (1989). Tectonic Discrimination of Granitoids. *Geol. Soc. Am. Bull.* 101, 635–643. doi:10.1130/0016-7606(1989)101<0635:tdog>2.3.co;2

Mirkamalov, R. K., Chirikin, V. V., Khan, R. S., Kharin, V. G., and Sergeev, S. A. (2012). *Results of U-Pb (SHRIMP) Datings of Granitoid and Methamorphic Complexes of the Tien Shan Folded belt (Uzbekistan). Bulletin of St. Petersburg University. Earth Sciences*. 7 (1), 3–25. (in Russian with English abstract).

Nabatian, G., Jiang, S.-Y., Honarmand, M., and Neubauer, F. (2016). Zircon U-Pb Ages, Geochemical and Sr-Nd-Pb-Hf Isotopic Constraints on Petrogenesis of the Tarom-Olya Pluton, Alborz Magmatic belt, NW Iran. *Lithos* 244, 43–58. doi:10.1016/j.lithos.2015.11.020

Padilha, D. F., Bitencourt, M. d. F., Nardi, L. V. S., Florisbal, L. M., Reis, C., Geraldes, M., et al. (2019). Sources and Settings of Ediacaran post-collisional Syenite-Monzonite-Diorite Shoshonitic Magmatism from Southernmost Brazil. *Lithos* 344-345, 482–503. doi:10.1016/j.lithos.2019.06.004

Paton, C., Woodhead, J. D., Hellstrom, J. C., Hergt, J. M., Greig, A., and Maas, R. (2010). Improved Laser Ablation U-Pb Zircon Geochronology through Robust Downhole Fractionation Correction. *Geochem. Geophys. Geosyst.* 11, a–n. doi:10.1029/2009GC002618

Pe-Piper, G., Piper, D. J. W., Koukouvelas, I., Dolansky, L. M., and Kokkalas, S. (2006). Postorogenic Shoshonitic Rocks and Their Origin by Melting Underplated Basalts: The Miocene of Limnos, Greece. *Geol. Soc. America Bull.* 121, 1–54. doi:10.1130/B26317.1

Pearce, J. A., Harris, N. B. W., and Tindle, A. G. (1984). Trace Element Discrimination Diagrams for the Tectonic Interpretation of Granitic Rocks. *J. Petrology* 25 (4), 956–983. doi:10.1093/petrology/25.4.956

Pearce, J. A. (1982). Trace Element Characteristics of Lavas from Destructive Plate Boundaries. *Orog. Andesites Relat. Rocks*, 528–548.

Peccerillo, A., and Taylor, S. R. (1976). Geochemistry of Eocene Calc-Alkaline Volcanic Rocks from the Kastamonu Area, Northern Turkey. *Contr. Mineral. Petrol.* 58, 63–81. doi:10.1007/BF00384745

Qi, L., Hu, J., and Gregoire, D. C. (2000). Determination of Trace Elements in Granites by Inductively Coupled Plasma Mass Spectrometry. *Talanta* 51, 507–513. doi:10.1016/S0039-9140(99)00318-5

Safonova, I., Biske, G., Romer, R. L., Seltmann, R., Simonov, V., and Maruyama, S. (2016). Middle Paleozoic Mafic Magmatism and Ocean Plate Stratigraphy of the South Tianshan, Kyrgyzstan. *Gondwana Res.* 30, 236–256. doi:10.1016/j.gr.2015.03.006

Sang, M., Xiao, W., Bakirov, A., Orozbaev, R., Sakiev, K., and Zhou, K. (2017). Oblique Wedge Extrusion of UHP/HP Complexes in the Late Triassic: Structural Analysis and Zircon Ages of the Atbashi Complex, South Tianshan, Kyrgyzstan. *Int. Geology. Rev.* 59, 1369–1389. doi:10.1080/00206814.2016.1241163

Sang, M., Xiao, W., Orozbaev, R., Bakirov, A., Sakiev, K., Pak, N., et al. (2018). Structural Styles and Zircon Ages of the South Tianshan Accretionary Complex, Atbashi Ridge, Kyrgyzstan: Insights for the Anatomy of Ocean Plate Stratigraphy and Accretionary Processes. *J. Asian Earth Sci.* 153, 9–41. doi:10.1016/j.jseaes.2017.07.052

Sang, M., Xiao, W., and Windley, B. F. (2020). Unravelling a Devonian-Triassic Seamount Chain in the South Tianshan High-pressure/ultrahigh-pressure Accretionary Complex in the Atbashi Area (Kyrgyzstan). *Geol. J.* 55, 2300–2317. doi:10.1002/gj.3776

Schaarschmidt, A., Klemd, R., Regelous, M., Voudouris, P. C., Melfos, V., and Haase, K. M. (2021). The Formation of Shoshonitic Magma and its Relationship to Porphyry-type Mineralisation: the Maronia Pluton in NE Greece. *Lithos* 380-381, 105911. doi:10.1016/j.lithos.2020.105911

Seltmann, R., Konopelko, D., Biske, G., Divaev, F., and Sergeev, S. (2011). Hercynian post-collisional Magmatism in the Context of Paleozoic Magmatic Evolution of the Tien Shan Orogenic belt. *J. Asian Earth Sci.* 42, 821–838. doi:10.1016/j.jseaes.2010.08.016

Şengör, A. M. C., Natal'In, B. A., and Burtman, V. S. (1993). Evolution of the Altaid Tectonic Collage and Palaeozoic Crustal Growth in Eurasia. *Nature* 364, 299–307. doi:10.1038/364299a0

Sláma, J., Košler, J., Condon, D. J., Crowley, J. L., Gerdes, A., Hanchar, J. M., et al. (2008). Plešovice Zircon - A New Natural Reference Material for U-Pb and Hf Isotopic Microanalysis. *Chem. Geology.* 249, 1–35. doi:10.1016/j.chemgeo.2007.11.005

Stern, R. J., Bloomer, S. H., Lin, P.-N., Ito, E., and Morris, J. (1988). Shoshonitic Magmas in Nascent Arcs: New Evidence from Submarine Volcanoes in the Northern Marianas. *Geol* 16, 426–430. doi:10.1130/0091-7613(1988)016<0426:sminan>2.3.co;2

Sun, S.-s., and McDonough, W. F. (1989). Chemical and Isotopic Systematics of Oceanic Basalts: Implications for Mantle Composition and Processes. *Geol. Soc. Lond. Spec. Publications* 42, 313–345. doi:10.1144/GSL.SP.1989.042.01.19

Tang, G.-J., Chung, S.-L., Hawkesworth, C. J., Cawood, P. A., Wang, Q., Wyman, D. A., et al. (2017). Short Episodes of Crust Generation during Protracted Accretionary Processes: Evidence from Central Asian Orogenic Belt, NW China. *Earth Planet. Sci. Lett.* 464, 142–154. doi:10.1016/j.epsl.2017.02.022

Thompson, J. M., Meffre, S., and Danyushevsky, L. (2018). Impact of Air, Laser Pulse Width and Fluence on U-Pb Dating of Zircons by LA-ICPMS. *J. Anal. Spectrom.* 33, 221–230. doi:10.1039/C7JA00357A

Turner, S., Arnaud, N., Liu, J., Rogers, N., Hawkesworth, C., Harris, N., et al. (1996). Post-collision, Shoshonitic Volcanism on the Tibetan Plateau: Implications for Convective Thinning of the Lithosphere and the Source of Ocean Island Basalts. *J. Petrology* 37, 45–71. doi:10.1093/petrology/37.1.45

van Hunen, J., van den Berg, A. P., and Vlaar, N. J. (2004). Various Mechanisms to Induce Present-Day Shallow Flat Subduction and Implications for the Younger Earth: a Numerical Parameter Study. *Phys. Earth Planet. Interiors* 146, 179–194. doi:10.1016/j.pepi.2003.07.027

Whalen, J. B., Currie, K. L., and Chappell, B. W. (1987). A-type Granites: Geochemical Characteristics, Discrimination and Petrogenesis. *Contrib. Mineral. Petrol.* 95, 407–419. doi:10.1007/Bf00402202

Windley, B. F., Alexeiev, D., Xiao, W., Kröner, A., and Badarch, G. (2007). Tectonic Models for Accretion of the Central Asian Orogenic Belt. *J. Geol. Soc.* 164, 31–47. doi:10.1144/0016-76492006-022

Windley, B. F., and Xiao, W. (2018). Ridge Subduction and Slab Windows in the Central Asian Orogenic Belt: Tectonic Implications for the Evolution of an Accretionary Orogen. *Gondwana Res.* 61, 73–87. doi:10.1016/j.gr.2018.05.003

Worthington, J. R., Kapp, P., Minaev, V., Chapman, J. B., Mazdab, F. K., Ducea, M. N., et al. (2017). Birth, Life, and Demise of the Andean-Syn-Collisional Gissar Arc: Late Paleozoic Tectono-Magmatic-Metamorphic Evolution of the Southwestern Tian Shan, Tajikistan. *Tectonics* 36, 1861–1912. doi:10.1002/2016TC004285

Wu, F.-Y., Yang, Y.-H., Xie, L.-W., Yang, J.-H., and Xu, P. (2006). Hf Isotopic Compositions of the Standard Zircons and Baddeleyites Used in U-Pb Geochronology. *Chem. Geology.* 234, 105–126. doi:10.1016/j.chemgeo.2006.05.003

Xiao, W., Windley, B. F., Allen, M. B., and Han, C. (2013). Paleozoic Multiple Accretionary and Collisional Tectonics of the Chinese Tianshan Orogenic Collage. *Gondwana Res.* 23, 1316–1341. doi:10.1016/j.gr.2012.01.012

Xiao, W., Windley, B. F., Sun, S., Li, J., Huang, B., Han, C., et al. (2015). A Tale of Amalgamation of Three Permo-Triassic Collage Systems in Central Asia: Oroclines, Sutures, and Terminal Accretion. *Annu. Rev. Earth Planet. Sci.* 43, 477–507. doi:10.1146/annurev-earth-060614-105254

Yan, Z., Chen, L., Xiong, X., Wang, K., Xie, R., and Hsu, H. T. (2020). Observations and Modeling of Flat Subduction and its Geological Effects. *Sci. China Earth Sci.* 63, 1069–1091. doi:10.1007/s11430-019-9575-2

Yang, H., Xiao, W., Sang, M., Mamadjanov, Y., Zhang, H., Zhang, Z., et al. (2020). Age and Petrogenesis of the Gabbros from Tajik South Tianshan:

Implications for Early Paleozoic Geodynamic Evolution of the Southwestern Central Asian Orogenic Belt. *Lithosphere* 2020, 7866431. doi:10.2113/2020/7866431

Zaprometov, M. E., Nosova, V. I., and Pominalny, V. I. (1973). "Geological Prognostic Map of the North-Eastern End of the Mogul-Tau Mountains," *Report of the Muzbek detachment No.15 for 1966-1973* (Adrasman town), 376. (in Russian)

Zhang, X.-Z., Wang, Q., Dong, Y.-S., Zhang, C., Li, Q.-Y., Xia, X.-P., et al. (2017). High-Pressure Granulite Facies Overprinting during the Exhumation of Eclogites in the Bangong-Nujiang Suture Zone, Central Tibet: Link to Flat-Slab Subduction. *Tectonics* 36, 2918–2935. doi:10.1002/2017TC004774

Zhao, X.-B., Xue, C.-J., Chi, G.-X., Mo, X.-X., Nurtaev, B., and Zhang, G.-Z. (2017). Zircon and Molybdenite Geochronology and Geochemistry of the Kalmakyr Porphyry Cu-Au deposit, Almalyk District, Uzbekistan: Implications for Mineralization Processes. *Ore Geology. Rev.* 86, 807–824. doi:10.1016/j.oregeorev.2017.04.008

Zu, B., Seltmann, R., Xue, C., Wang, T., Dolgopolova, A., Li, C., et al. (2019). Multiple Episodes of Late Paleozoic Cu-Au Mineralization in the Chatkal-Kurama Terrane: New Constraints from the Kuru-Tegerek and Bozymchak Skarn Deposits, Kyrgyzstan. *Ore Geology. Rev.* 113, 103077. doi:10.1016/j.oregeorev.2019.103077

Conflict of Interest: The authors declare that the research was conducted in the absence of any commercial or financial relationships that could be construed as a potential conflict of interest.

Publisher's Note: All claims expressed in this article are solely those of the authors and do not necessarily represent those of their affiliated organizations, or those of the publisher, the editors and the reviewers. Any product that may be evaluated in this article, or claim that may be made by its manufacturer, is not guaranteed or endorsed by the publisher.